Master's thesis

NTNU
Norwegian University of Science and Technology
Faculty of Information Technology and Electrical Engineering
Department of Electric Power Engineering

Sindre Austad

HTS Winding Design and 3D FEA Modeling of Superconducting Machine for Aviation

Master's thesis in Electric Power Engineering
Supervisor: Jonas K. Nøland
Co-supervisor: Runar Mellerud og Christian Hartmann
July 2023

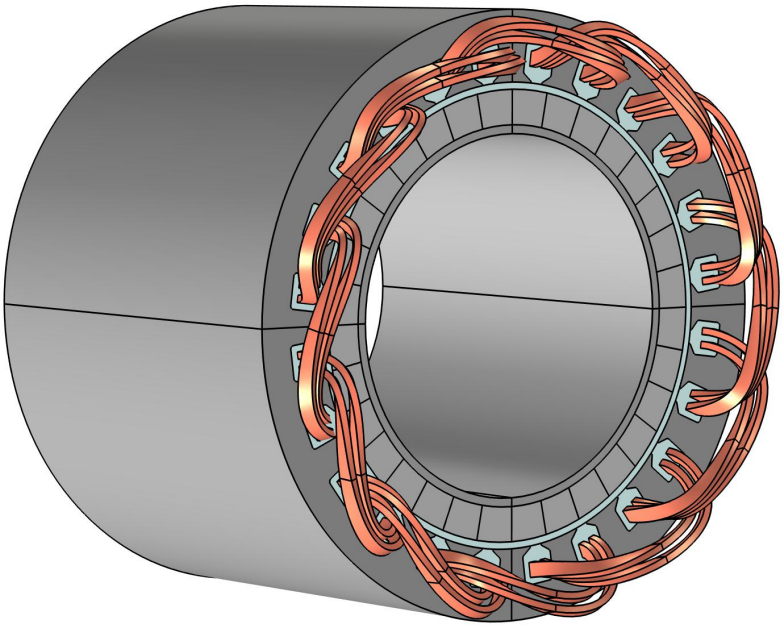

NTNU
Norwegian University of
Science and Technology

Sindre Austad

HTS Winding Design and 3D FEA Modeling of Superconducting Machine for Aviation

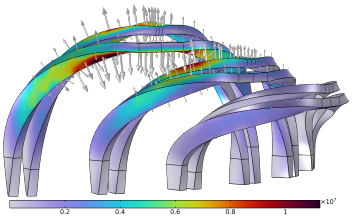

Master's thesis in Electric Power Engineering
Supervisor: Jonas K. Nøland
Co-supervisor: Runar Mellerud og Christian Hartmann
July 2023

Norwegian University of Science and Technology
Faculty of Information Technology and Electrical Engineering
Department of Electric Power Engineering

NTNU
Norwegian University of
Science and Technology

HTS Winding Design and 3D FEA modeling of Superconducting Machine for Aviation

Sindre Austad
Department of Electric Energy,
NTNU
Trondheim, Norway

***Abstract*—In this thesis, methods and formulations for the modeling of rotating machinery are presented. Models are developed in 3D of an SCM for Aviation using the commercial FEA software Comsol Multiphysics. 3D models enable the study of more complex geometries such as end-windings which cannot be easily represented in 2D. The HTS tapes have a high angular sensitivity to magnetic fields and are susceptible to degradation from deformation. 3D models make it possible to validate winding designs to ensure the integrity of the tapes prior to implementation. The 3D modeling threshold can be high for a novice, and there are very few guides and examples available. In this thesis, the most important steps and formulations are explained throughout the process of modeling the SCM for aviation, as a reference and guide for future modeling endeavors. A short investigation of the possibility of including complex superconductive behavior of the HTS coils using the 3D homogenized T-A formulation is undertaken. End windings are then designed and implemented in Comsol to include the modeling of complex geometries, and to create a foundation for later end winding designs. Differences in formulations required for different studies are investigated, and a model including a segmented Halbach array is modeled with respect to magnet losses. An initial analysis of the impact of the end-winding on the HTS tapes is made, with focus on magnetic flux penetration in the normal direction with resulting Lorentz forces, and some possible implications are discussed. A skewed saddle coil design is shown to give promising initial results with low harmonic disturbance, and is recommended for in-depth study in the future. An analysis of magnet losses with respect to segment length is also undertaken, and shorter segments are found to give significantly lower losses, with a close to inversely exponential relationship between segment length and loss for the lengths studied. Losses are found to be Magnet losses are also found to be skewed in favor of magnets of a certain magnetization direction, giving an asymmetrical loss for the rotor, and a 49-65% higher than average loss for the north pole depending on segment length.**

***Index Terms*—HTS, 3D, Modeling, Design, End Winding, FEA, Comsol, Saddle Coil, Magnet segmentation, Lorentz force,**

I. Introduction

THE process of electrification is in full progress around the globe, and is affecting and changing most industries. The aviation industry remains almost untouched by global efforts to replace fossil fuels as the main source of energy, and challenges still remain. Aviation is a cut-throat industry, with some of the lowest profit margins and lowest returns on investments of any industry in the world (approximately 1.1$ profit per passenger as of 2023 [1]), making it a highly incentive-based industry [2], [3]. Attempts by airlines to reduce emissions have been focused on increasing fuel efficiency, cutting weight, offsetting, and other measures that are at least as related to increase in profit as reduction of emissions. Airlines do not produce their own fuel nor aircraft, and only have opportunity to cut emissions marginally; airlines are therefore calling on the aircraft manufacturers to assume some of the responsibility [1].

The number of large aircraft manufacturers in the world is low, and just a handful of these could change the direction of the industry quickly. But historically, there has been little incentive to improve and reinvent in the commercial sector due to high demand for existing products, and research and development traditionally being focused on military applications. However, recent technological advancements and the growing interest from the public have made a wider range of current and near-future options increasingly attractive, leading to a technology race between the largest aircraft manufacturers, such as Boeing and Airbus [4], [5]. Over the past few years, interest and research in electrical and hybrid alternatives to combustion engines has grown many-fold, and optimism in the field is rising [6], [7]. Electrical airplanes already exist, but are limited in range and capacity due to the large weight-to-power ratio of electrical machines. The power density of combustion engines, and the energy density of fossil fuels still outcompetes electrical machines [8]. Thus, a revolution in electrical propulsion is inevitable in order to achieve full electrification of the aviation industry. One of the biggest hopes and possibilities for achieving the needed increase in power-to-weight ratio is the superconductor (SC) [6], [7].

Superconductors far exceed the capabilities of conventional conductors like copper and aluminum and can carry a much greater current at zero losses, which gives the opportunity to push the efficiency and power density beyond current limits [9]. Superconductors have been around since the early 1900s, but have until recent years been an unrealistic option due to extreme temperature requirements and high cost. Previous production has also been limited in capability due to material challenges and especially in the production of useful lengths, but new advancements in high-temperature superconductors (HTS) have lowered the requirements and cost of SCs and widened the range of possible applications [10], [11], making

them a realistic alternative for propulsion machines. Several types of HTS are now being produced at lengths and in shapes that are increasingly applicable, at a higher scale, making the technology more available for new markets, such as aviation and the transport industry in general [11].

The electrification of the aviation industry plays an important role in reaching the goals of reducing human-induced emission of greenhouse gasses. Through the Clean Aviation initiative and Flightpath 2050, the European Union and partners have set a goal of reaching net-zero climate emissions for all flights by 2050 [12], [13]. This thesis is a part of the effort to reach and exceed these goals through the development of a superconducting machine (SCM) by the Team Aviation research group at the Cryo-Electric Aviation Laboratory (CEAL) at the Norwegian University of Science and Technology (NTNU) [14], [15].

The work is still at an early stage at CEAL, and the focus for Team Aviation is currently on design and modeling of superconductors with related cabling methods and cooling systems, and the initial cryogenic testing of practical solutions. The author had the pleasure of being part of the first in-house cryogenic tests as part of a specialization project in preparation for this thesis [16]. In the specialization project, a study was conducted to investigate some key factors of coil manufacturing with HTS tapes, focusing mainly on development of terminations for the tapes and general testing methods, culminating in the cryogenic testing of the terminations. The project report contained information relevant to this thesis and [16] is therefore referred to throughout the text.

The focus of this thesis is the development of 3D models to study the behavior of a machine based on a proposed SCM for aviation designed by Mellerud Et Al in [14], using the finite element analysis (FEA) tool Comsol Multiphysics®. The aim is to demystify the 3D modeling process and enable a new dimension of modeling and analysis, both figuratively and literally, for members of TEAM Aviation and other similar projects through the inclusion of more complex parts of the machine such as the end-windings. Studies have already been conducted for the proposed machine using 2D FEA, but results are not yet verified in 3D, and some important aspects that are unavailable in 2D are still missing [14]. One such aspect is the behavior of HTS tapes in complex geometries as in the curves associated with the end windings. The electromagnetic properties of superconducting materials are known to be altered when exposed to stress from deformations and the impact of stress may impose constraints on machine design and lead to future design changes [17]. Another design constraint comes from the flat shape of the conductor, which significantly limits the possible end-winding configurations and geometries. For this purpose, two end-winding designs were developed and implemented in 3D models of the SCM. Methods for the creation of these end windings were also developed and described to enable use by others in the future.

Many of the aspects of HTS tapes in windings require specialized formulations to be modeled accurately. To address this, the implementation of a popular homogenized 3D **T-A** formulation for HTS tapes was tested by replicating its original implementation in [18]. This formulation models the current distribution and effects of magnetic fields more accurately than methods with lossless coils commonly used for rotating machinery. The application of SC models in 3D also gives the opportunity to study other aspects such as losses, cooling requirements and termination methods in depth, which can enhance the machine design through a higher degree of accuracy in future studies. To ensure that the modeling process is relevant in its descriptions, the 2D SCM by [14] was used as a case study throughout the thesis, and is finally analyzed with respect to end windings, magnet losses and some general performance parameters. The rest of the thesis is divided into the following sections:

- section II includes a short introduction of the SCM designed in [14], which all models in this thesis are based on. Relevant design parameters for the machine are presented, along with performance parameters from the 2D analysis conducted in [14].
- section III gives some theoretical background on superconductors with a focus on the HTS tapes featured in the windings SCM. A short overview of some formulations used to model superconductors with FEA in 3D is given, before the choice is settled on the Homogenized 3D **T-A** formulation. The steps involved in the implementation of the formulation in Comsol are described, before an unsuccessful attempt is made at replicating a study where the formulation was successfully implemented on a stack of HTS tapes in a racetrack coil. Finally, the results from the attempt is presented and compared to the original study, and a separate replication of the original, and some of the issues and possible causes for the failure are discussed.
- section IV focuses on the windings of the machine, and the challenges related to the use of HTS tapes in coils. Two possible end winding designs developed for the SCM are presented, both of which are variants of the saddle coil. Some of the implications of the designs are discussed, before the methods and geometry used to develop and model the coils in Comsol are described, along with a general formula developed to model saddle coils with a high level of detail. The end winding models are then included in 3D models using the machine geometry, and later used to study the effects of the different designs.
- In section V, the process and methods for modeling of rotating machinery in 3D are described. A description of the mixed formulation that combines the magnetic vector potential, $\vec{A}$, and the magnetic scalar potential φ_m is given, along with an overview of the variations and combinations that can be used to study different aspects of the machine. The variations are then described in greater detail for each for some common studies of a

machine.

- In section VI, the models developed and described in section V are analyzed with respect to the different studies described in the same section, with main focus being on the end windings and magnet losses in the machine.
- section VII includes a discussion of some of the issues that have arisen during the work for this thesis, in section VIII, a conclusion and recap of the thesis is made, before some of the steps on the road ahead for the 3D modeling of the SCM are listed in section IX.

II. The Superconducting motor

The superconducting machine modeled in this thesis is based on the preliminary machine design originally presented in [15] and further developed in [14]. The machine is a three-phase superconducting surface mounted permanent magnet machine with 8 poles and 24 stator slots.

The stator windings are distributed superconducting windings with ReBCO (Rare-earth Berium Copper Oxide) superconductors in the form of HTS tapes from Shanghai Superconducting Technology Company Ltd. (SHSC). The ReBCO tapes of the machine are copper plated tapes of the YBCO variant with Yttrium as the superconducting rare-earth metal layer [19]. The windings have a coil span of three slots, and two series connected coils per slot with 7 turns per coil. The HTS tapes are parallel in each slot, with the face pointing in the radial direction to minimize the impact of flux leakage across slots. The rotor has NdFeB BMN-46EH magnets arranged in a Halbach array consisting of 4 magnets per pole. The magnets are intended to be divided into segments in the axial direction to reduce the magnet losses due to eddy currents, which is a topic of section VI. The stator is made from laminated $0.2\,\mathrm{mm}$ sheets of Vacoflux 50 steel, the permanent magnets in the rotor are NdFeB BMN-46EH. Each slot has two coils per slot with 7 turns per coil, giving a total of 14 turns per slot. Some relevant design parameters can be seen in Table I.

TABLE I: Design parameters for SCM from [14]

Parameter	Symbol	Value	Unit
Number of slots	N_s	24	-
Number of poles	p	8	-
Outer diameter	D_o	346	mm
Air gap diameter	D_{ag}	260	mm
Active length	L	240	mm
Air gap length	g	4	mm
Magnet length	l_m	20	mm

A number FEM studies have already been conducted by [14] for the SCM design, using a cross-section of the machine for analysis in 2D. The performance parameters seen in table I was obtained from the 2D studies, which was the benchmark for the 3D models in this thesis. The design of the machine itself is not within the scope of this thesis, and [14] is referred to for a more detailed description of the machine geometry and materials, as well as a thorough 2D analysis of the machine and superconductors.

TABLE II: Performance parameters from 2D analysis by [14].

Parameter	Symbol	Value	Unit
Average mechanical power	P_{mech}	2500	kW
Rotational speed	n	5000	rpm
Electrical frequency	f_{el}	333.3	Hz
Phase voltage (rms)	U_{ph}	421	V
Applied phase current (rms)	I_{ph}	683	A
Power factor	$cos(\phi)$	0.725	
Average torque	T	4776	Nm
Steel losses	P_{steel}	1497	W
Active HTS losses @40 K	P_{HTS}	788 -1574	W
Efficiency estimate	η	99.8	%

Several 3D models were developed in COMSOL Multiphysics for this thesis based on the descriptions given in this section, and according to the requirements of the studies of interest.

III. Superconductors

The machine described in the previous section is designed around superconducting windings [14]. The type of SC chosen for the machine is ReBCO. ReBCO SCs are Type II superconductors produced as tapes, usually referred to as HTS tapes, consisting of a stack of layers, often coated with copper. The stacks contain a superconducting ceramic layer made of rare earth metals, such as Yttrium, Gadolinium, Europium, etc. [20], [21]. The superconducting layer is usually surrounded by silver, substrate, and stabilizing layers in different configurations depending on the producer [16], [19].

Superconductors are materials with the ability to conduct electricity with zero resistance and loss of energy. The phenomenon of superconductivity is explained by the Meissner effect which occurs when superconducting materials are cooled to below their critical temperature (T_c). Below the critical temperature, the material enters a superconductive state also known as the Meissner state, where external magnetic fields are expelled from its interior, up to a point. When a superconductor is exposed to a magnetic field, the field strength decreases exponentially as a function of the penetration depth from the surface into the conductor, leading to a very small penetration depth for the field [22]. In a type II SC, magnetic fields can still exist within the conductor in the superconductive state, which is called flux trapping and occurs when a magnetic field is applied before and during cool-down to its critical temperature [23], [24].

Based on the characteristics exhibited as the breakdown of superconductivity occurs, superconductors can be distinguished into two types: Type I and Type II. Type I superconductors are fully superconductive until the critical limits of temperature, field, or current are reached, at which point they

immediately revert to the normal state and act as conventional conductors [22], [25]. When the limits of Type II superconductors are exceeded, they enter a transition state called the mixed state, in which partial flux penetration occurs. When the field enters the surface of the superconductor, it induces a circulating vortex of supercurrent consisting of electron pairs (Cooper pairs), called a fluxon or Abrikosov vortex. The trapped flux in a type II SC is also conserved in the form of a fluxon. As one of the critical parameters increases, so does the number of vortices and flux lines penetrating the surface. The regions of the conductor that experience flux penetration exist in the normal resistive state between the remaining superconductive regions, which gives the name of the mixed state [26], [27]. Initially, when the conductors enter the mixed state, these vortices are located at pinning centers where they are prevented from moving by a pinning force. When a transport current is applied to a superconductor, the current and the magnetic field set a Lorentz force ($F = J \times B$) acting on the vortices; If the Lorentz force exceeds the pinning force, the vortices are forced to move from their previously pinned location, resulting in what is known as flux creep [28]. The motion of the vortices as a result of an applied force means that work is being done and energy is being released, resulting in resistive areas in the conductor [22]. At this point, the Meissner state has broken down and the conductor exists in the mixed state [22], [26], [29]. When the current or field increases, the superconductive regions are gradually displaced until current must pass through a region existing in the resistive state. As the current in a superconductor carries more energy than the material is able to dissipate in its resistive state, heat increases, causing the critical limits to be exceeded in an event called quenching, in which superconductivity is completely lost. If the current is large enough, the energy can be released in a more dramatic fashion with a small explosion.

The real critical values of field (H_c) and current (I_c) for a superconductor are found at the point of equilibrium between the Lorentz and pinning forces. The pinning forces preventing the breakdown of superconductivity are dependent on the microstructure of the superconducting layer, leading most producers to optimize for pinning and thereby increasing the critical limits. Deformations common in windings may lead to defects in the microstructure, which result in reduced electrical properties. The critical limits of the conductors are interdependent, and an increase in temperature, field, or current, leads to a reduction of the other two. Due to interdependence, a small defect could dramatically affect the overall performance of the conductors, and subsequently the machine [22], [29].

A. 3D HTS formulations for FEM

To eventually be able include the full behavior of superconducting windings in rotating machinery, a study was undertaken to investigate the possibility of implementing a superconductor formulation in complex 3D geometries. A few methods of modeling HTS tapes using FEM were investigated before a choice was made; Among these are the H-formulation, **T-A** formulation, and MEMEP (minimum electromagnetic entropy production), all of which focus solely on the superconducting layer. The H-formulation, first developed in [**?**], was the first of these and has been the method of choice until the **T-A** formulation was later developed in [30]. The computational efficiency varies between the formulations; The H-formulation is reported to be the most computationally heavy and difficult to implement of the three; The **T-A** formulation is found to be more efficient and easier to implement than the H-formulation [18], [30]; MEMEP was found to be much more efficient than the H- and **T-A** formulations, but is also the most recent of the three and has yet to be tested on complex geometries, and at this moment it has only been used to study demagnetization of trapped fields in superconductors [31]. Due to the efficiency and proven application to complex 3D geometries, the **T-A** formulation was chosen for further study.

Two different ways to model a coil with the **T-A** formulation have emerged as candidates for effective 3D modeling of HTS tapes. One is a *full* model, where all the conductors and turns of the coil are represented [30]. Another is a homogenized model, where the coil is represented as an anisotropic bulk that can reproduce the magnetic behavior of the coil as a whole. Due to the number of conductors in the windings of the SCM described in section II, the approach chosen was based on the 3D homogenization of the **T-A** formulation by Vargas-Llanos et al. in [18], which was developed from the *full* 3D **T-A** formulation first introduced by Zhang et al. in [30]. The major difference between the full and homogenized approaches is that the full formulation uses a 2D surface to model an individual conductor, while the homogenized formulation uses a 3D domain to model the entire winding. Both formulations use a thin strip approximation, where only the superconducting layer is considered, which limits their ability to model AC losses significantly. AC losses are highly dependent on the non-superconducting layers, especially in high-frequency applications such as an SCM for propulsion, since these are more prone to eddy currents. The homogenized formulation is even less reliable with respect to AC losses, since interactions between tapes in a homogenized coil are ignored [18].

Homogenization does, however, provide an efficient way to investigate the effect of magnetic fields on the current density of the coil, especially in the more complex geometries which are often required in the end windings. The homogenization significantly simplifies the modeling process, from modeling and implementing the formulation on each conductor individually, to all conductors simultaneously [18]. The homogenized model is also easier to implement for complex geometries in Comsol; Since Comsol is not able to sweep a 1D curve, a 2D surface must be defined by extruding or revolving the 1D curve, or by parametric surfaces. Extrusion and revolutions are simple to use but limit the geometrical complexity to straight lines or perfectly circular shapes. Parametric surfaces have

very few limitations, but can be hard and very time-consuming to define in the shape of windings. The homogenized approach does not have this problem, and thus the end windings can simply be swept along a 3D defined curve, as explained in more detail in section IV.

Many of the descriptions of the **T-A** formulation and its implementation in 3D are often ambiguous and take some of the steps in the process for granted; Most studies have little or no additions, and are close to exact reiterations of the descriptions used in the original full 3D formulation of [30] and homogenization of [18]. An attempt was therefore made to lay out the equations and information needed to implement the **T-A** formulation in 3D from the literature, and explain some of the steps and reasoning throughout the process by replicating the 3D homogenization of the **T-A** formulation implemented by [18] on a racetrack coil.

At the end of this section, it can be seen that the replication was not fully successful, most likely due to incorrect boundary conditions. Initial values were undefined for the current vector potential within the superconducting domain, and a solution could not be found when vertical mesh elements were included in the model, which indicated an error in the formulation. The model was thus unable to capture the characteristic distribution of current density expected for the width of the coil, despite giving a reasonable distibution over the height. However, the process and method used in this thesis are hoped to be clear enough for the error to be identified and corrected in the future.

*B. The **T-A** formulation*

The **T-A** formulation is an efficient method used to model superconductors with FEM tools such as Comsol Multiphysics. The method applies the **T** formulation only to the superconducting regions and the **A** formulation to all regions to find a solution to the finite element problem. The formulations are based on the current and magnetic vector potentials, **T** and **A**, respectively. In general, the current potential **T** is defined by the current density as:

$$\vec{J} = \nabla \times \vec{T} \tag{1}$$

The potentials, **T** and **A**, are coupled by using the potential T to calculate the electric field E, and the potential **A** to calculate the magnetic field B in Maxwell-Faraday's law, which is the governing equation for the **T**-formulation:

$$\nabla \times \vec{E} = \frac{\partial \vec{B}}{\partial t} \tag{2}$$

where E and B are calculated from the potentials **T** and **A** according to eq 3 and 4, respectively:

$$\vec{E} = \rho(\nabla \times \vec{T}) \tag{3}$$

$$\vec{B} = \nabla \times \vec{A} \tag{4}$$

In the **T-A** formulation, the relationship between the electric field and current is given by the E-J power law, which is a model used to simulate the increasing resistivity of the superconducting material in the mixed state as the current increases. This model uses a constant, E_0 or E_c, which indicates the electrical field of the superconductor at the critical current, this value is often set to $0.1\,\mathrm{mV/m}$ in models, as well as by superconductor manufacturers when estimating the critical limits of the conductor. The E-J power law is defined as:

$$\vec{E} = E_0 \left| \frac{\vec{J}}{J_c(\vec{B})} \right|^{(n-1)} \frac{\vec{J}}{J_c(\vec{B}} \tag{5}$$

where $\vec{J}$ is the current density in the conductor, n is a value that represents the steepness of the curve when plotting the relationship between $\vec{J}$ and $\vec{E}$, and $J_c(\vec{B})$ is the critical current density of the conductors as a function of the magnetic field $\vec{B}$, defined by:

$$J_c(B_\parallel, B_\perp) = \frac{J_{c0}}{\left[1 + \sqrt{\left(B_\parallel \cdot k\right)^2 + \left(\frac{B_\perp}{B_c}\right)^2}\right]^b} \tag{6}$$

where b and k are curve-fitting coefficients based on the superconductive characteristics of HTS tapes in magnetic fields [18], [32], [33]. The equation for $J_c(\vec{B})$ is called the modified Kim-model, which is a model used to determine the degradation of the critical current density seen in HTS tapes, due to weakened pinning forces from increased interactions between vortices in the superconducting ceramic layer when exposed to magnetic fields from different directions [34]–[36].

The thin-sheet approximation is usually used for the conductors in the **T-A** formulation; Due to high width-to-thickness ratio, the thickness of the conductors can be collapsed to a thin sheet consisting of only the superconducting material. It then follows that current can only flow in the thin sheet, in the direction parallel to the surface of the tape, and hence the current vector potential is only considered in the direction normal to the surface [18], [30], [37]. $\vec{T}$ can then be considered as a scalar, T, with direction $\vec{n}$:

$$\vec{T} = T \cdot \vec{n} \tag{7}$$

In a 2D, or a straight rectangular 3D coil, the normal direction would be parallel with one of the Cartesian coordinates, which would simplify the equations significantly, but in order to model complex 3D geometries, the normal direction must follow the geometry and all components of the normal vector

must be included. With **T** only in the normal direction, the current density is expressed as:

$$\begin{bmatrix} J_x \\ J_y \\ J_z \end{bmatrix} = \begin{bmatrix} \frac{\partial(Tn_z)}{\partial y} - \frac{\partial(Tn_y)}{\partial z} \\ \frac{\partial(Tn_x)}{\partial z} - \frac{\partial(Tn_z)}{\partial x} \\ \frac{\partial(Tn_y)}{\partial x} - \frac{\partial(Tn_x)}{\partial y} \end{bmatrix} \tag{8}$$

Since the HTS tapes are approximated to be infinitely thin sheets, the magnetic flux is only considered in the direction normal to the surface of the conductor, and the flux density parallel to the sheet is ignored. Applying this to Faraday's law gives:

$$\begin{bmatrix} \frac{\partial(E_z)}{\partial y} - \frac{\partial(E_y)}{\partial z} \\ \frac{\partial(E_x)}{\partial z} - \frac{\partial(E_z)}{\partial x} \\ \frac{\partial(E_y)}{\partial x} - \frac{\partial(E_x)}{\partial y} \end{bmatrix} \cdot \begin{bmatrix} n_x \\ n_y \\ n_z \end{bmatrix} + \begin{bmatrix} \frac{\partial(B_x)}{\partial t} \\ \frac{\partial(B_y)}{\partial t} \\ \frac{\partial(B_z)}{\partial t} \end{bmatrix} \cdot \begin{bmatrix} n_x \\ n_y \\ n_z \end{bmatrix} = 0 \tag{9}$$

Using the relationships defined by equations 5-9, the formulation can be implemented in Comsol Multiphysics with the *Coefficient Form PDE* and the *Magnetic Fields* modules.

1) Defining a custom coordinate system in Comsol: As previously mentioned, the **T-A** formulation requires a normal vector to be defined along the entire geometry of the coil. For the full model, this is not an issue; The normal and tangential directions in Comsol are well defined on the surfaces of an object, regardless of its geometry. Unfortunately, no definition of the normal direction exists within the domains of the object, and the normal direction has to be defined manually. To achieve this, the *Curvilinear Coordinates* module (CC) in Comsol was utilized. This is a separate module that models the flow in a domain from input to output surfaces. By choosing a domain, and defining an input and output surfaces, the direction of flow between the two surfaces is found and stored as a vector field which can be used as a coordinate system in other studies. A disadvantage in Comsol is that the curvilinear is not able to to determine more than one direction at once, which means that two different CC modules must be used in Comsol to define a coordinate system. The normal vector can be found with only one CC module, but a full coordinate system enables more opportunities. Luckily, a third module is not needed, since CC has the option of creating a base vector system, where a user defined vector can be chosen as the second basis vector. The steps required to define a custom coordinate system in Comsol are listed here:

- Add two *Curvilinear Coordinates* modules to the *Model Builder* from the *Mathematics* interface, CC1 and CC2, and select only the coil domain for both.
- Make sure *Normalize vector field* is enabled. This creates a normalized unit vector for the directions.
- Add a *Diffusion Method* node to both CC1 and CC2 and select only the coil domain for both.

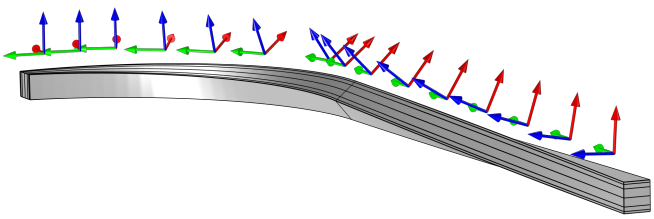

Fig. 1: Curvilinear coordinate system for twisted and bent coil.

- Add an *Inlet* and *Outlet* node to the *Diffusion Method* node of CC1.
- Select the coil surface from which the normal direction should be defined as the *Outlet*, and the opposing surface as the *Inlet*.
- Add an *inlet* and *outlet* node is added to the *Diffusion Method* node of CC2.
- Select the surface at one end of the coil as *Inlet* (preferably the current input), and the other as *Outlet*.
- Run a *Stationary Study* with default solver settings.This is needed the field vectors of CC1 to be an option for *Second basis vector* selection in CC2.
- When the study is finished, the normal vector from CC1 should be stored as the vector [cc.Vx, cc.Vy, cc.Vz].
- In CC2, a select *user defined* for the *Second basis vector*, and enter each component of the stored normal vector into its respective Cartesian coordinate.
- Enable *Create base vector system* in CC2.
- Rerun the same *Stationary Study*, including both CC modules.
- When the study is finished, a coordinate system following the geometry is stored. The coordinate system can be accessed in the *definitions* node in Comsol, and each vector component should also be accessible as variables with the names [cc1.eix, cc1.eiy, cc1.eiz], where i indicates the vector: i = 1 is the tangential to the length, i = 2 is the normal, i = 3 is the tangential to the width.

After obtaining the curvilinear coordinate system, the individual components were renamed to fit their respective directions and simplify the reference. The tangential to the length was renamed $\vec{e_1}$, the tangential to the width as $\vec{e_2}$, and the normal direction as $\vec{N}$, as seen for $\vec{N}$ in eq. (10):

$$\begin{bmatrix} N_x \\ N_y \\ N_z \end{bmatrix} = \begin{bmatrix} cc1.e2x \\ cc1.e2y \\ cc1.e2z \end{bmatrix} \tag{10}$$

One of the advantages of CC is that this operation can be done for several geometries at once, so a custom coordinate system for a complete machine winding can be defined for all phases simultaneously by following the steps listed here.

2) T-formulation in Comsol: In this thesis, the physics module, *Magnetic Fields* (MF) was used for the **A**-formulation, as the magnetic vector potential is well defined by default. $\vec{A}$ is

also defined in the *Rotating Machinery, Magnetic* module used for the SCM in later sections, which can be used implemented the formulation in the same way. The **T**-formulation was implemented by adding a *Coefficient Form PDE* module from the *Mathematics* interface. In the *Coefficient Form PDE*, **T** was defined as a dependent variable, T, with unit $[\mathrm{A/m}]$, and the source term was given the unit $[\mathrm{T/s}]$. The equation defining the PDE of this module with the dependent variable T is given as:

$$\begin{aligned} e_a \frac{\partial^2 T}{\partial t^2} + d_a \frac{\partial T}{\partial t} + \nabla \cdot (-c\nabla T - \alpha T + \gamma) + \\ \beta \cdot \nabla T + aT = \quad f \end{aligned} \tag{11}$$

The PDE is used to define the relationship in equation (9). Using the normal vector, $\vec{N}$, defined by the CC, the components of the current density were defined as variables based on equation (8). By omitting the current density vector $\vec{J}$ from the E-J power law in equation (5), a variable resistivity, independent of direction, ρ, was used to define each component of $\vec{E}$ independently, to later simplify the curl operation in eq. (9):

$$\rho = \frac{E_0}{J_c(\vec{B})} \left| \frac{\vec{J}}{J_c(\vec{B})} \right|^{(n-1)} \tag{12}$$

The parallel and perpendicular magnetic fields needed for $J_c(\vec{B})$ in eq. 6 were found using the dot product of the magnetic field from the *Magnetic Fields* module, and the new unit vectors defined by CC. The variable names have been altered to some extent for readability. The components of the magnetic field also include the index "mf.", which is ignored here.

$$\begin{aligned} B_\perp &= \vec{B} \cdot \vec{N} \\ B_\parallel &= \vec{B} \cdot \vec{e_1} + \vec{B} \cdot \vec{e_2} \end{aligned} \tag{13}$$

Using resistivity ρ and current density $\vec{J}$, each component of the field $\vec{E}$ was defined as an individual variable:

$$\begin{aligned} E_x &= \rho J_x \\ E_y &= \rho J_y \\ E_y &= \rho J_z \end{aligned} \tag{14}$$

From the relationship defined in eq. (9), it can be seen that when only the field in the normal direction is considered, the expression becomes the first order partial differential equation:

$$\begin{aligned} \left(\frac{\partial(E_z)}{\partial y} - \frac{\partial(E_y)}{\partial z} \right) N_x \left(\frac{\partial(E_x)}{\partial z} - \frac{\partial(E_z)}{\partial x} \right) N_y + \\ \left(\frac{\partial(E_y)}{\partial x} - \frac{\partial(E_x)}{\partial y} \right) N_z + \frac{\partial(B_x)}{\partial t} N_x + \\ \frac{\partial(B_y)}{\partial t} N_y + \frac{\partial(B_z)}{\partial t} N_z = \quad 0 \end{aligned} \tag{15}$$

This expression can be manipulated to fit the Coefficient Form PDE. By setting all coefficients in the PDE to zero, except the source term, f, and the vector of the conservative flux source, γ, in eq.(11), the equation becomes:

$$\nabla \cdot \gamma = f \tag{16}$$

Since the respective components of $\vec{N}$ are not dependent on the variables derivated for in the divergence of γ, but the the components of $\vec{E}$ are, the components of $\vec{N}$ are thus considered as constants, and hence the left side of the equation can be used to find the curl of the electric field:

$$\nabla \cdot \begin{bmatrix} E_y N_z - E_z N_y \\ E_z N_x - E_x N_z \\ E_x N_y - E_y N_x \end{bmatrix} = -\frac{\partial B_x}{\partial t} N_x - \frac{\partial B_y}{\partial t} N_y - \frac{\partial B_z}{\partial t} N_z \tag{17}$$

By writing out the full differential equation and factoring out the constants in eq.(17), i.e. the components of $\vec{N}$, the final equation becomes equal to Faraday's law in eq.(15). The components of the vector seen on the left side of eq.(17) was entered into the conservative flux source, γ, to obtain the relationship defined by Faraday's law. The final Coefficient Form PDE was applied to all superconducting domains.

3) Coupling with A-formulation: In the PDE implemented for the vector potential, A is coupled with T in the T-formulation, but to properly implement the **T-A** formulation, T must also be coupled with A in the A-formulation through Maxwell-Ampere's Law (18):

$$\nabla \times \left(\frac{1}{\mu} \nabla \times \vec{A} \right) = \vec{J} \tag{18}$$

where $\vec{J}$ is the current density defined by the current vector potential according to eq.(8). With the thin-strip approximation in the homogenized coil approach, the thickness of the superconducting layer, δ, is collapsed, and a unit cell is defined around the superconductor. This unit cell has the height, Λ, which is the height of the HTS tape when all layers are included. The current density in the superconducting layer is then distributed over the cross section of the HTS tape, by scaling the current according to eq. (19) [18]:

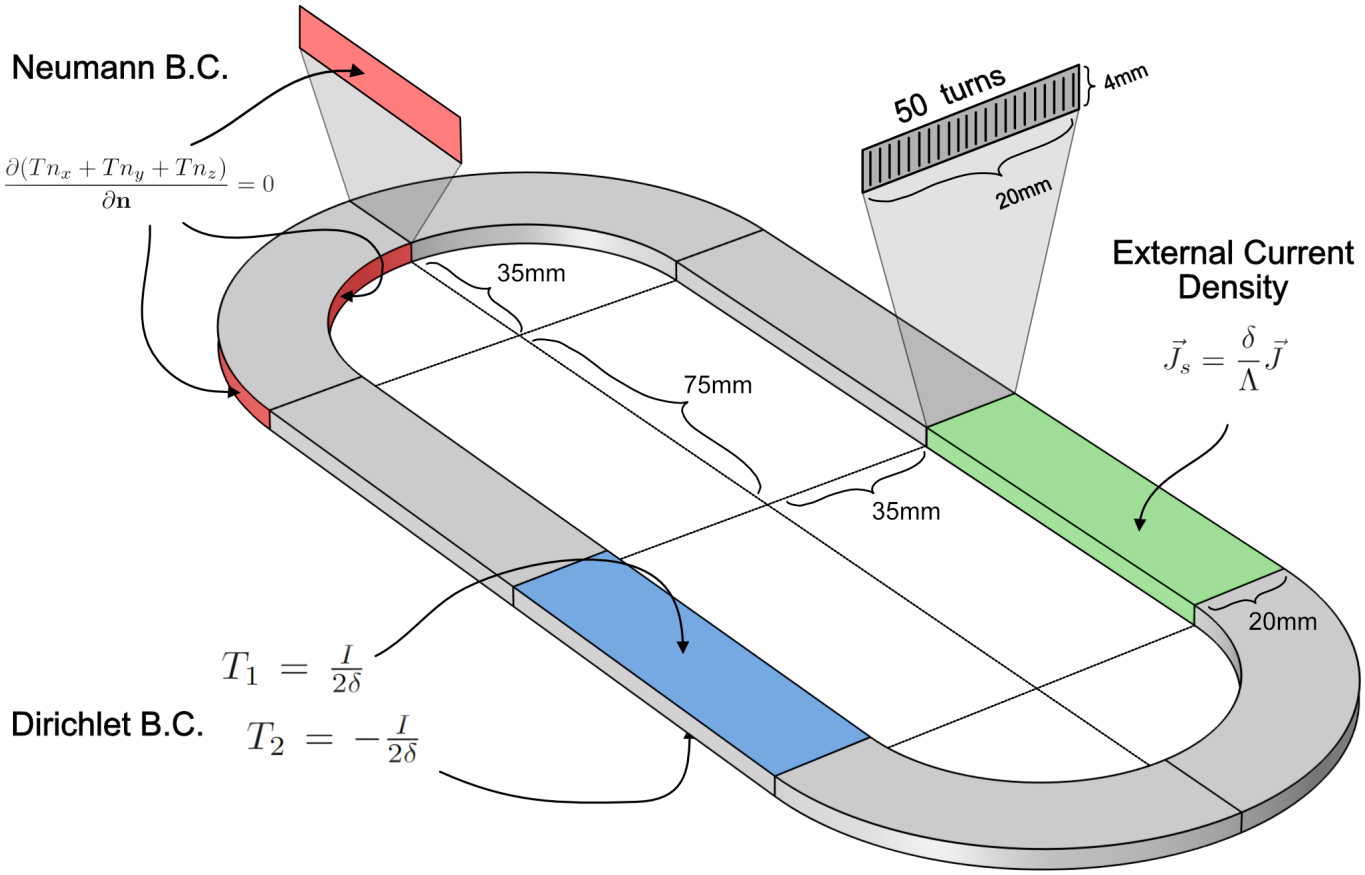

Fig. 2: Geometry and constraints of homogenized **T-A** formulation on the superconducting domain, for replication of Vargas-Llanos et. al. [18]. Dirichlet on sides of coil; Neumann on top and bottom of coil (inner and outer surface); External Current Density in whole domain. The same conditions are used around the whole quarter coil section used, and not only the sections indicated. The exception is the Zero flux Neumann Condition, which is only implemented on the cross section at the symmetry boundaries.

$$\vec{J}_s = \frac{\delta}{\Lambda}\vec{J} \tag{19}$$

The current density can then be applied either by introducing the scaled current density $\vec{J}_s$ from eq.(19) to the A-formulation as an applied external current density $\vec{J}_e$ in the whole superconducting domain [18], [37], or by introducing it as an applied surface current density on the sides of the stack, $\vec{J}_{se}$ [38]:

$$\begin{aligned} &\text{Domain:} \quad \vec{J}_e = \vec{J}_s \\ &\text{Surface:} \quad \vec{J}_{s0} = \vec{J}_s \cdot \delta \end{aligned} \tag{20}$$

where the external current density in the domain is directly applied to the A-formulation through equation (21) with an *External Current Density* node, and the surface current density as the boundary condition seen in equation (22) with the *Surface Current Density* node:

$$\vec{J} = \sigma\vec{E} + \vec{J}_e \tag{21}$$

$$\vec{n} \times \left(\vec{H}_1 - \vec{H}_2\right) = \left(\vec{n} \times \vec{J}_{s0}\right) \times \vec{n} \tag{22}$$

Two separate materials were used for the superconducting and nonsuperconducting domains. The default *Air* material from Comsol was used in both cases, but with zero conductivity in the superconducting domains and non-zero conductivity in the non-superconducting domain, which is important since *Ampere's law* node uses the material conductivity to calculate current density with eq.(21); by setting the material conductivity, the first term on the right side of eq.(21) disappears, and as a result, only the current density defined by the T-formulation is used.

To solve the finite element problem using the **T-A** formulation, boundary conditions must also be defined. The thin-strip approximation uses the assumption that the superconducting sheets in the coil are densely packed with the same current

flowing in every sheet [18]. Since the same current is flowing in all sheets, the integral of the current density over any cross section along the length of the coil should be equal to the applied current [30]:

$$I = \iint_S \vec{J} dS = \oint_L \vec{T} ds = (T_1 - T_2) \cdot \delta \tag{23}$$

where T_1 and T_2 is the current vector potential on either side of the stack, and δ is the height of the conductor [30]. The transport current can then be imposed by defining the current vector potential with *Dirichlet Boundary Conditions* in the boundaries representing the tightly stacked tape edges on either side of the coil, so that eq.(23) is satisfied. Here, this was done with $T_1 = \frac{I}{2\delta}$ and $T_2 = -\frac{I}{2\delta}$ on either side (the same sides as the surface current density if $\vec{J_{s0}}$ was used).

4) Neumann boundary Condition: In the **T-A** formulation, Neumann boundary conditions, also called second-order boundary conditions, are required on particular surfaces of the coil. A Neumann condition was placed on the input and output boundaries on the ends of the coil with a *Zero Flux* node, as described in [37]. Neumann conditions must also be added to the top and bottom surfaces of the coil (outer and inner surfaces in Figure 2) [18], [37]:

$$\frac{\partial(T_x n_x + T_x n_y + T_y n_z)}{\partial \mathbf{n}} = 0 \tag{24}$$

However, it is not completely obvious how this condition should be implemented; During the implementation of the **T-A** formulation in this thesis, several variations of the Neumann conditions were tested with no luck. The initial attempts focused on the condition on the form seen in eq.(24). Which is implemented with the *Flux/Source* node in Comsol:

$$-\mathbf{n} \cdot (-c\nabla T - \alpha T + \gamma) = g - qT \tag{25}$$

where γ is the only non-zero coefficient from the PDE, qT was set to zero, and the source term was set to $g = T \cdot N_x + T \cdot N_y + T \cdot N_z$ for the particular solution seen later in this section. The other variations of g tested for the Neumann Condition can be seen in Section VII. Due to the lack of success, a different approach was tested. In [39] it is said that in the 3D T-A model, the tangential components of the electric field from the A-formulation have contributions to the Neumann condition:

$$\int \vec{E} \times \delta\vec{T} \times (d\mathbf{A}) \tag{26}$$

and that these boundary conditions represent a new coupling effect for the **T-A** formulation. It is further said that for the *Full* **T-A** formulation in 3D, this can be implemented in Comsol by an additional Dirichlet condition on one of the surfaces, with

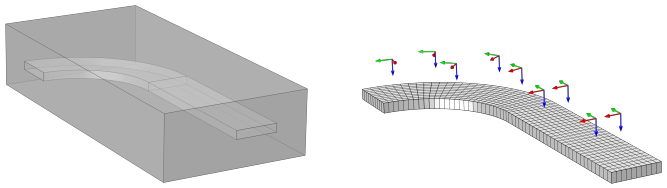

(a) Geometry with surrounding air domain (70x150x30mm). Symmetry planes of superconducting domain are flush with boundary of surrounding air.

(b) Curvilinear coordinates and mesh. Only horizontal mesh distribution was possible within domain. 10x60 mesh elements SC domain.

Fig. 3: Geometry of model used to replicate [18].

input $T = 0$, and a flux condition, with input: $Ex \cdot e1x + Ey \cdot e1y + Ez \cdot e1z$, where the electric field is calculated using the **A**-formulation with the *Magnetic Fields* module, and not from the **T**-formulation as previously. The flux condition in question is assumed to be the *Flux/Source* node. Although [39] only specifies that this method can be used for the full formulation, it was also tested for the homogenized formulation here, but did not correct the problem. The final method presented here used equation (24) implemented with equation (25), with $g = T \cdot N_x + T \cdot N_y + T \cdot N_z$.

5) Validation: The previously described implementation was tested by replicating the study conducted by Vargas-Llanos et al. in [18] on a simple race track coil before moving on to more complex geometries. The same geometry and parameters were used, with the exception of the n-value and mesh distribution, which were not stated in the study. The value was therefore chosen to be $n = 25$, and the mesh was as seen in Figure 3b. Based on The coil consisted of 50 turns of a REBCO HTS tape, deformed with out-of-plane to form a racetrack coil (Figure 2).

TABLE III: T-A parameters

Name	Value
b	0.6
k	0.275
f	50 Hz
n	25
I_c	160 A
I_{peak}	100 A
E_0	$1 \cdot 10^{-4}$ V/m
J_{c0}	49 GA/m^2
B_{c0}	$32.5 \cdot 10^{-3}$ T
h_{sc}	1 µm
w_{sc}	4 mm

where I_{peak} is the peak value of the applied current, E_0, J_{c0}, B_{c0} are rated values for a tape with critical current $I_c = 160$ at 77 K self-field, b and k are curve-fitting coefficients based on experimental data from [33]. All values were found in [18]. h_{sc} and w_{sc} are the height and width of the superconducting layer, respectively.

From Figure 4 it is clear that the normalized current density

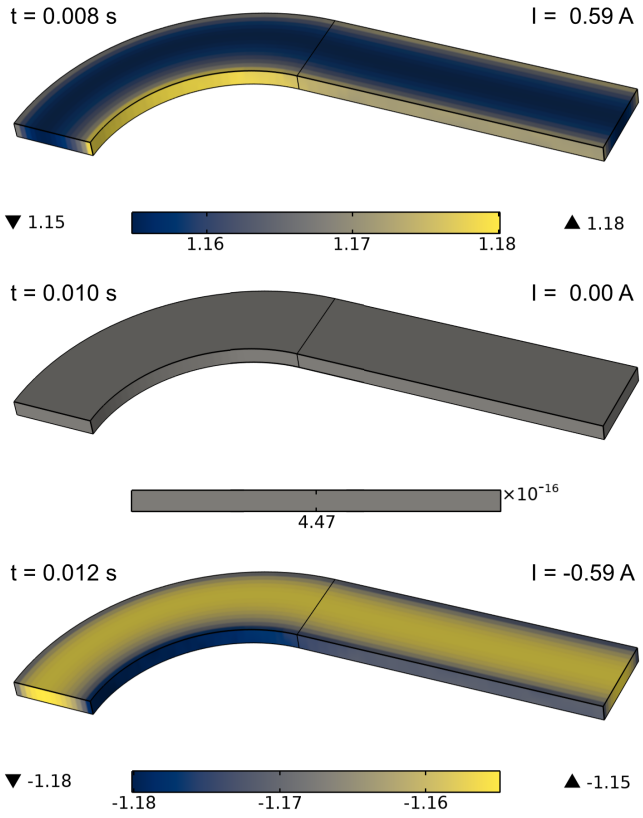

Fig. 4: Plot of normalized current density $\vec{J}/J_c(\vec{B})$. Only distribution in height of coil is visible.

distribution is not as expected for the homogenized 3D **T-A** formulation for HTS tapes, and the results do not agree with what is reported in [18]. A major difference can be seen at t = 0.0 in, where the current is approximately zero, equally distributed over the volume, while the normalized current density for the same time-step in [18] ranges from -1.5 on the edges, to 1.5 approximately $1\,\mathrm{mm}$ from the edge in the width direction, before reaching 0 in the center of the width. The reason the difference is likely the issue previosly mentioned, where a solution could only be found with vertical mesh elements. Since there is no information from mesh nodes within the domain about the current density in the width, Comsol uses interpolation to represent the volume, which gives a uniform current density over the width. The distribution in the height of the coil is more promising for $t = 0.008\,\mathrm{s}$ and $t = 0.012\,\mathrm{s}$ in Figure 4; The current density was found to be slightly higher toward the outermost tapes on the top and bottom of the coil, which is a behavior commonly found in stacks of HTS tapes. The distribution also differs between the inner and outer edges of the curved part for these timesteps, which is expected [18], [32]. In [18], however, this behavior was also found when the current was zero, at $t = 0.01\,\mathrm{s}$, after a half cycle at $50\,\mathrm{Hz}$, which was not the case here.

The flux density also differs greatly from [18] and a

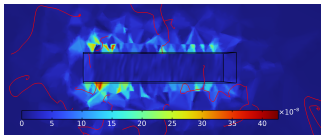

(a) $|\vec{B}|$ at t = 0.010 s, when I = 0 after half cycle.

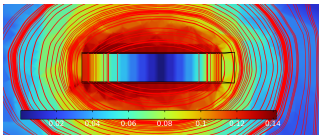

(b) $|\vec{B}|$ at t = 0.015 s, when I = 100 A after 3/4 cycle (I_{peak}).

Fig. 5: Magnetic flux density norm $|\vec{B}|$.

replication of the same study in [40], where the maximum value was found to be $0.25\,\mathrm{T}$ in the straight section of the superconducting domain, and is heavily skewed towards the inner tapes of the coil. In Figure 5b it can be seen that the flux density is also skewed towards the inner tapes of the coil (left edge in Figure 5) but to nowhere near the extent found in [40], and with a much lower maximum value of approximately $0.14\,\mathrm{T}$.

*6) Final remarks on the implementation of the homogenized 3D **T-A** formulation:* The method of implementation described in this section was not successful. As initially stated, many of the steps involved in the implementation are taken for granted in the literature, leaving room for the wrong interpretations to be made, which seems to have occurred in this case. The author suspects the Neumann boundary condition to be the main contributor, but errors may also have occurred in other steps, and corrections must be made in the future.

IV. Windings

The orientation of the windings in slots is an important design feature for the machine, since it minimizes the flux leakage penetrating the tapes, thus reducing degradation of the superconductor properties. This does however create other challenges. The materials and shape of the conductors also impose constraints on the deformations, or geometrical transformations, which limits the possible end winding designs. This section aims to address these issues by a study of some of the design limitations for the SCM, and the development of a realistic winding design that is within these limits.

A. HTS winding challenges and limitation

The superconducting layer in REBCO HTS tapes is an extremely thin ceramic material, making it brittle and susceptible to damage. The electromagnetic properties of HTS tapes are highly dependent on the micro structure of its SC layer and a small damage can reduce and even eliminate superconductivity [11]. All types of strain experienced by the tape cause a material stress which can simultaneously compress and stretch its structure in different parts, altering the micro structure of the SC layer and its properties. The other layers around the SC stabilizes and shields it from some of the strain, which enables the HTS tape as a whole to be more flexible. This allows for some deformation without damaging it irreversibly. The

tapes are still, however, very limited compared to conventional conductors.

When the HTS tapes are shaped into coils they are displaced and deformed from their natural state, causing tension and strain which leads to a material stress. The most relevant stress for the end windings are the hoop stress, axial stress and radial stress from bending, as well as the shear stress from twisting. All of these impact and reduce the electromagnetic properties of the SC to some degree, and too large a stress could cause a complete loss of superconductivity. Comprehensive reviews of the electromechanical properties of REBCO HTS tapes, including of types of strain, and methods for calculating its effects on critical currents can be found in [10] and [11]. HTS tapes are also known to be negatively affected by exposure to magnetic fields. A combination of material stress and magnetic fields could seriously degrade the windings, leading to a lower rated machine. In the slots of the SCM, the stacks of HTS tapes are oriented with the thickness of each tape close to parallel with the field, in order to reduce exposure to the magnetic field. In the ends of the machine, however, exposure to the field is much harder to control since the windings of all phases must pass around one another in a distributed winding layout. This combination of stress- and field exposure often occurs in the end windings of the machine, where all of the deformation occurs and the windings are exposed to time-varying magnetic fields from several angles at once.

1) Bending and twisting: There are two relevant modes of bending for a tape shaped conductor, an in-plane-bend and out-of-plane bend (axial bend). The in-plane and out-of-plane bends are also referred to as "hard" and "easy" bends, respectively, based on the mechanical resistance of the tapes to each mode (Figure 6). The most simple and common winding design with HTS-tapes is the racetrack coil. A racetrack coil only requires an out-of-plane bend, which is unlikely to damage the conductors, and can be achieved by hand. Out-of-plane bends are the most common deformation of an HTS tape, being widely used in coil manufacturing for several applications [41]–[44]. Superconducting machines have already been produced with some success using racetrack coils, and more machines are currently in production [44]–[46]. The minimum bending radius in the in-plane direction for an HTS tape is often specified from the producer, while no information on in-plane bending is provided. For the specific HTS-tapes envisioned for the SCM, a minimum bending radius of $11-15\,\mathrm{mm}$ is given for the out-of-plane direction.

Superconducting coils with in-plane bends are currently not as common for rotating machinery, but are sometimes used in superconducting coils for particle accelerator magnets, which require a specific shape [41], [42], [47]. Because of the tape geometry, the "hard" bend is the deformation for which HTS tapes are most susceptible to damage, they therefore and require larger scales than that of the SCM modeled for here [48]. Tests of in-plane bends have shown that for REBCO tapes of $4\,\mathrm{mm}$, reversible reduction in critical current of up to 5% was measured at a critical bending radius of $250-280\,\mathrm{mm}$. Below this radius, the critical current degraded irreversibly [49]. An in-plane bend would provide the shortest path for the end windings, but as the straight-line distance between slots of the same winding in the machine is $111\,\mathrm{mm}$, this type of bend is out of the question. Bends similar to the in-shape bend can be made with a combination of twisting and out-of-plane bending, and minimum bending radius in this direction is well below what is needed in the machine.

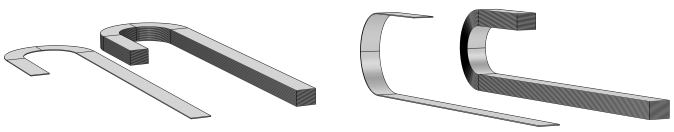

(a) In-plane bend. (b) Out-of-plane bend.

Fig. 6: Bending of a single conductor and a stack of conductors.

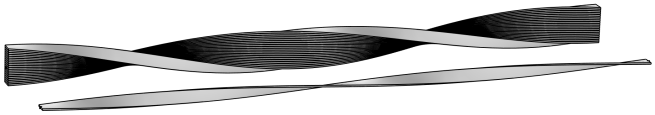

Fig. 7: A $200\,\mathrm{mm}$ twist pitch for single HTS tape and stack of tapes of $4\,\mathrm{mm}$ width (360° twist over $200\,\mathrm{mm}$).

2) Twisting: Since the windings have to enter and exit slots in the orientation to the field, they must be twisted by at least the angle corresponding to three slot pitches of a full coil span (45°), and likely more than this, since a transposition is required to complete the bend. In [50], the critical current was calculated analytically and tested experimentally for HTS tapes under different torsional strains. Both analytical and experimental results showed a sharp degradation of critical current for twist pitches below $130\,\mathrm{mm}$, but no significant reduction above this length. By assuming that the end winding is shaped in a perfect half circle, its length is found to be $175\,\mathrm{mm}$. To return to the same orientation relative to the slot, a minimum twist of angle $(45 + 180 \cdot n)^\circ$ is required from one slot to the next. In a regular saddle coil with $n = 0$, to avoid the "hard" bending direction, an overhang is usually created over the stator in order to obtain the shape through the "easy" bend. In the initial part of the overhang, the coil often twists outwards until it reaches the center of the coil, where it mirrors this transformation and twists back with the opposite angle. This gives an effective twisting angle greater than 45°, but still lower than coils with $n = 1$. A different solution is a half-transposed saddle coil ($n = 1$); Still working with the assumption that the end windings are perfectly circular, a twist pitch of $280\,\mathrm{mm}$ is found for end windings with this coil type, which is within the limits found in [50]. Following this reasoning, a full transposition end winding is also possible, but more than this, $n \geq 3$, would lead to degradation of the tapes and should be avoided.

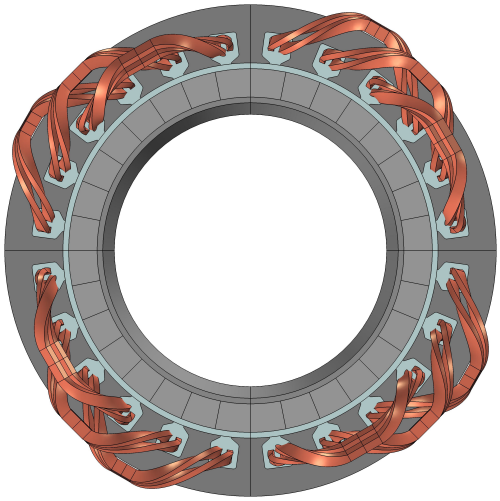

(a) Top view of rounded saddle winding. A pattern is visible from the different radial bend lengths.

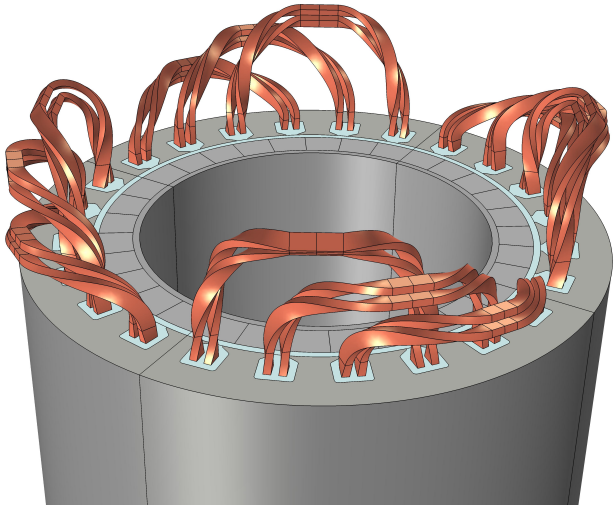

(b) Side view of end windings with saddle coils. Ordered counter clockwise by phase, from A to C and lowest to highest axial length.

Fig. 8: SCM with rounded saddle coil end winding design.

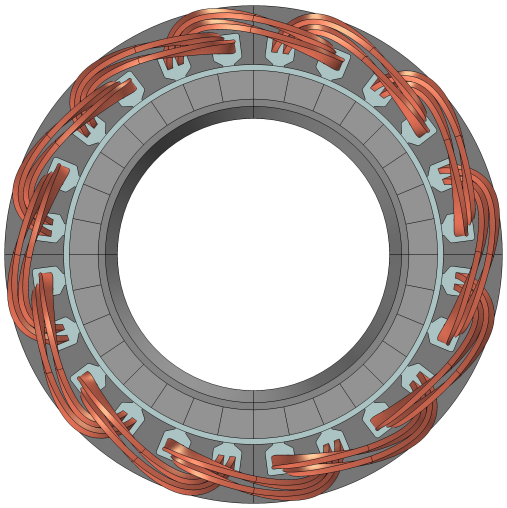

(a) Top view of skewed end winding. Compact and rotationally symmetric design.

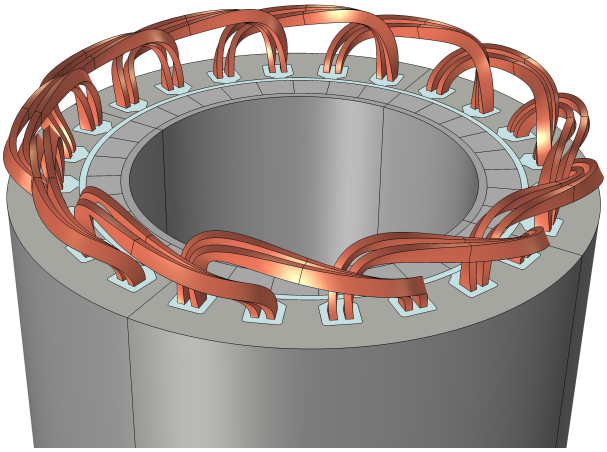

(b) Side view of skewed end winding. End windings of different phases overlap each other in the same manner.

Fig. 9: SCM with skewed saddle coil end winding design.

B. End winding design

Two different end windings were designed and implemented for the SCM in Comsol Multiphysics based on the limitations found for the conductors. Of the possibilities previously mentioned, one design is a common rounded saddle coil, and the other is a half-transposed and skewed rectangular saddle coil. The former is simply referred to as a rounded coil in this thesis, while the latter is referred to as a skewed coil. Here, the end windings are first presented, along with some discussion of the implications of each design, before the geometry of the windings is described, and finally the the end windings are implemented in Comsol. The end winding designs are later studied with respect to their impact on the machine in section VI.

1) Rounded saddle Coil: The rounded coil was developed based on the assumption that the natural bending and twisting of the conductor is the design with the least negative impact on the performance of the superconducting tapes. A flexible material exposed to a strain will, when unconstrained, change its geometry to minimize the amount of stress. By natural bending and twisting, the geometrical deformation that occurs when enforcing the placement only inside the slots is meant, i.e, the remaining end winding is free to move into position by itself. Since the material of the HTS tape is quite flexible to out-of-plane bending and torsion, this natural deformation can be significant when a high amount of stress is enforced on the straight part of the windings. The strain in the conductor causes the stack to both bend and twist outward from start to the centre of the end winding, and vice versa from the center

to the other end, to form a saddle coil.

Classical saddle coils do not lend themselves well in a distributed end winding sequence, since the coils of one phase would be placed in the path of the other phases. In a physical coil, this might not be as big an issue, since the coils can be insulated from each, but for modeling and simulation purposes, contact between domains of different phases must be avoided. To avoid direct contact in this formation, the end windings of different phases must have different lengths. The saddle coils developed in this thesis are therefore designed to mimic the natural deformation at different end winding heights. Proof of the exact geometrical behaviour of a coil of HTS tapes under stress is not provided in this thesis, and the design is based purely on practical experience from work with the conductors.

During previous practical and experimental experience with HTS tapes in [16], it was observed that a lower height in the axial direction causes a sharper bend with a greater length in the radial direction and lower degree of twisting; while a greater height in the axial direction causes a less sharp bend with a greater radius and larger degree of twisting. This means that by using different lengths to avoid contact, will give a unique end winding for each phase. The machine including end windings that mimic this behaviour can be seen in Figure 8.

One of the advantages of the saddle coil design is that it is simpler to manufacture, and easier to implement in the machine. There are also several disadvantages. The difference in geometry for the end windings of different phases makes it harder to create a compact design while avoiding contact between phases. The pattern of different heights repeats around the circumference and may lead to increased unwanted harmonics in the machine that could be avoided with a design where the coils of all phases are equal. This end winding design also includes an overhang which requires extra space at the ends of the machine.

2) Skewed saddle coil: The skewed saddle coil was developed to create a more compact and symmetrical solution than was possible with the common saddle coil described in the previous subsection. For the end windings to be symmetrical for all phases, the stacks of conductors must be wound around one another to avoid contact. To achieve this with rectangular stacks of flat conductors, the stacks must transposed either by half or full rotations, and bent into a slight S-shape using out-of-plane bends. The skewed saddle coil end winding can be seen in Figure 9. The ”skewed” part of the design comes both from the asymmetry seen from the top of the end windings (Figure 9a), and the asymmetry in the axial direction. To avoid contact, the end winding enters and leaves the slots closer to the stator one side than the other, which may also cause unwanted harmonics. In an attempt to lower the interference from the asymmetry, the end windings at opposing ends of the machine were reversed and oriented in opposite directions, giving the rhombus-like shape seen in Figure 14a and Figure 25.

This design may require more complicated holding and cooling mechanisms required around the end windings, due to the complex shape. The twisted shape is likely to give a non-uniform magnetic field density on the surface of the end windings, which may cause severe current density degradation and increase of AC losses in specific areas. This could also produce Lorentz forces that are hard to predict, which could mean that in depth studies are needed to properly design holding structures and reinforcement. As there is no difference between the phases, the design is expected to yield lower harmonic interference.

C. Coil geometry

Both of the end winding designs described here, are variations of a saddle coil. Saddle coils are not inherently difficult to model, and could be easily modeled with parametric or bezier curves, by sweeping a surface along a defined curve, as was done for the end windings here. Circular conductors are not dependent on twisting or bending direction, and these factors do not require any attention in the design process. The biggest challenge in the development of the coils was the rectangular shape of the stack of HTS tapes. Making the rectangular shaped coils move smoothly between slots while avoiding contact between phases and ensuring semi-realistic twisting and curvature proved a time-consuming task. In both cases, the 3D model of the machine was made including the conductors of a single slot. This provided the straight length of the winding, and also two surfaces from which to build the end windings. The rounded saddle coil was made with parametric curves, which provided the most customizable but time-consuming design, while the skewed coil was made with bezier curves, which was faster and more efficient. In addition to the two designs modeled here, the design of a general saddle coil which can be used to model and study windings in greater detail is also included.

1) General saddle coil: A general formula for a saddle coil was first made to accommodate modeling of each individual parallel conductor in all series connected turn and coil in the windings, but the level of detail was superfluous for the studies conducted in this thesis, and was not included in the final models used for analysis. A simplified version of the general saddle coil was later used for the rounded saddle coil, and the general could give a good background for the modeling of the rounded coil. The definition of the general coil could also be very useful for in depth study of the interaction between turns in individual sections of the winding or the winding as a whole.

The design was made by splitting a ellipsoid into 8 sections to represent the saddle shape seen in Figure 10, and defining a separate parametric curve for each section. From Table IV-C1, it can be seen that some of the expressions are the same for all coordinates; The eight curves could also be represented

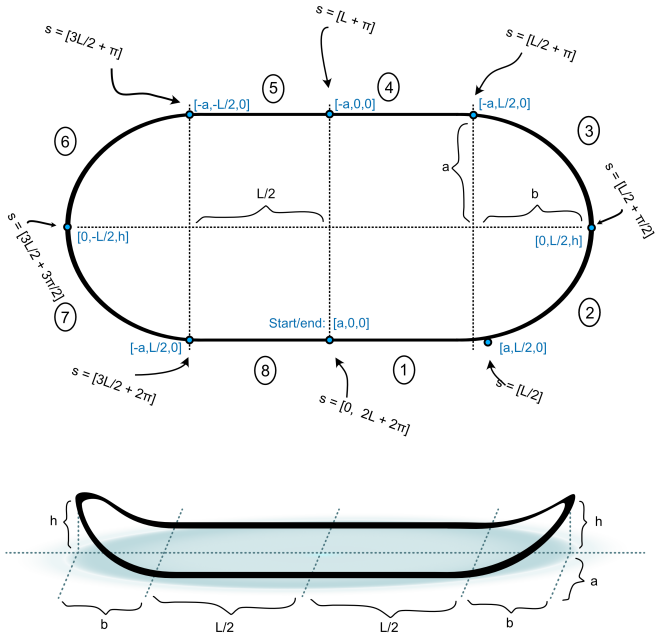

Fig. 10: Saddle coil measurements with parametric curve intervals for first turn in coil.

by only 3 curves, but splitting into more sections gives better control of the twisting needed in the ends of the saddle coil. The choice of curves should be based on the requirements, and if only three curves are needed, curves 1 and 8, 2 and 3, as well as 6 and 7, can be combined by simply extending the interval limits.

The major and minor radii of the ellipsoid, a and b, represent the center distance between slots and the end winding height in the axial direction, respectively. The length L is the machine length, h is the height of the end winding bend in the radial direction, and s is the parameter defining the curves in the interval between two points. For the radial bends, an additional exponent is added to be able to adjust the sharpness of the bend with the parameter s_b. This method was found to good results for $2 < s_b < 4$. Two additional terms, $\frac{s \cdot d}{2(\pi+L)}$ and $(d \cdot i)$, are also included in the expression for the z-direction to increase the height of the coil by a distance d so that additional turns are stacked on top of each other. The parameter i is the current turn, and the first turn is indicated by $i = 0$. These two terms can be ignored for a flat saddle coil. A good value for d would be the center distance between two turns:

$$d = (h_{hts} + \delta_{hts}) \cdot n_{hts} + \delta_{turns} \tag{27}$$

where h_{hts} is the height of a single conductor, δ_{hts} is the free distance between conductors in parallel, n_{hts} is the number of conductors in a single turn, and δ_{turns} is the free distance between two turns. The parametric curves describing this coil can be seen in Table IV-C1. It should be mentioned that in order to properly include twisting at the ends of the coil, an additional term should be added to the y-coordinate for each turn, as is done with the z-direction.

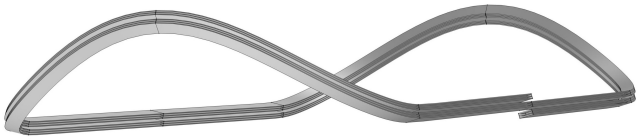

Fig. 11: General saddle coil modeled with parametric curves from Table IV-C1 (two turns, three parallel conductors).

2) Rounded saddle coil: As mentioned previously, the rounded saddle coil (Figure 8) is a simplified version of the general saddle coil. The rounded coil was intended to be implemented as a single homogeneous bulk, and the level of detail given by modeling each individual conductor was not required. Because of this, the rounded coil was modeled as a flat coil by setting the terms $\frac{s \cdot d}{2(\pi+L)} + (d \cdot i)$ equal to zero for all curves. Since there was no gradual increase in height along the length of the winding, the coil became symmetric at the center, making it possible to model the end winding using only half the coil. The models intended for study of the end winding design also included only one of the end windings, which enabled the modeling of the curved part to be done using only Curve 2 from Table IV-C1. The straight section of three coils inside their respective slots were modeled through an extrusion of the machine cross-section which included the placement of the conductors within the slots. Both the rounded and general saddle coil are best suited in a concentrated winding layout; one of the biggest issues with this design was that the SCM in [14] uses a distributed layout, hence different lengths were needed for the end windings to avoid contact. To be able to control the end winding to a larger degree, an extra length was modeled outside the slot by using Curve 1 (Table IV-C1) and setting $L = L_e$, where L_e is the additional straight length before bending starts. A set of these 2 curves were made for all three phases, and each phase was given its own set of parameters for individual modification. In the earliest models made with this coil design, a set of curves and parameters was made for each of the two coils in each slot, and each parameter had to be adjusted individually for all 6 coils. It was eventually discovered that that a both coils could be made with a single set of parametric curves if perfectly centered between the two coils, which simplified the process significantly. During the process, it was also found that changing the sign of the twisting direction in the curved part of the coil gave a sharp and oddly shaped edge at the center of the end winding. To circumvent this, a straight curve with length w_m was added to center of the end winding, making up a part of its width.

The major radius, a, was calculated by finding the center distance between two slots of the same phase, s_{cc} and setting $a = \frac{s_{cc}}{2}$. Using arbitrary values for the remaining parameters, the curves were then rotated and displaced so that the straight section was directed entirely in the axial direction of the

TABLE IV: Parametric Curve Expressions and Interval Limits

Parametric Curve	Expression			Interval limits	
	x	y	z	Min	Max
Curve 1	a	s	$\frac{s\cdot d}{2(\pi+L)} + (d\cdot i)$	0	$\frac{L}{2}$
Curve 2	$a\cos(s-\frac{L}{2})$	$b\sin(s-\frac{L}{2})+\frac{L}{2}$	$h\cdot\left\lvert\sin(s-\frac{L}{2})\right\rvert^{s_b+\left\lvert\sin(s-\frac{L}{2})\right\rvert} + \left(\frac{s\cdot d}{2(\pi+L)} + (d\cdot i)\right)$	$\frac{L}{2}$	$\frac{L}{2}+\frac{\pi}{2}$
Curve 3	$a\cos(s-\frac{L}{2})$	$b\sin(s-\frac{L}{2})+\frac{L}{2}$	$h\cdot\left\lvert\sin(s-\frac{L}{2})\right\rvert^{s_b+\left\lvert\sin(s-\frac{L}{2})\right\rvert} + \left(\frac{s\cdot d}{2(\pi+L)} + (d\cdot i)\right)$	$\frac{L}{2}+\frac{\pi}{2}$	$\frac{L}{2}+\pi$
Curve 4	-a	$L+\pi-s$	$\frac{s\cdot d}{2(\pi+L)} + (d\cdot i)$	$\frac{L}{2}+\pi$	$L+\pi$
Curve 5	-a	$L+\pi-s$	$\frac{s\cdot d}{2(\pi+L)} + (d\cdot i)$	$L+\pi$	$L+\pi$
Curve 6	$a\cos(s-\frac{3L}{2})$	$b\sin(s-\frac{3L}{2})-\frac{L}{2}$	$h\cdot\left\lvert\sin(s-\frac{3L}{2})\right\rvert^{s_b+\left\lvert\sin(s-\frac{3L}{2})\right\rvert} + \left(\frac{s\cdot d}{2(\pi+L)} + (d\cdot i)\right)$	$\frac{3L}{2}+\pi$	$\frac{3L}{2}+\frac{3\pi}{2}$
Curve 7	$a\cos(s-\frac{3L}{2})$	$b\sin(s-\frac{3L}{2})-\frac{L}{2}$	$h\cdot\left\lvert\sin(s-\frac{3L}{2})\right\rvert^{s_b+\left\lvert\sin(s-\frac{3L}{2})\right\rvert} + \left(\frac{s\cdot d}{2(\pi+L)} + (d\cdot i)\right)$	$\frac{3L}{2}+\frac{3\pi}{2}$	$\frac{3L}{2}+2\pi$
Curve 8	a	$s-2(L+\pi)$	$\frac{s\cdot d}{2(\pi+L)} + (d\cdot i)$	$\frac{3L}{2}+2\pi$	$2(L+\pi)$

machine, before the set of curves belonging to each phase was finally rotated by the slot pitch θ_s multiplied with the integer, into their respective slots. The curve parameters for each phase were then adjusted manually, before sweeping the faces of the coil section along the parametric curves. Due to symmetry, only half the coil was modeled using a sweep, and the remaining half using using a mirror-operation on with the face of the half end winding as mirror surface (Figure 12). During the sweeping process, twisting was enabled in the settings of the *Sweep* operation in Comsol for the first and second sections, which twists the swept surface along the curve with an angle defined as a function of a parameter, s. A twist constant, α, was added in order adjust the twist to mimic the combination of bending and twisting needed, so that the twist angle was defined as $-s\cdot\alpha$. The third section left without twisting for a smooth transition into the mirrored opposite half. The first section was given a low value of α for the gradual twist of the coil out of the slots, and the second was given a higher value for the twist of the bending part. Finally, the parameters for radius, bending height, sharpness, and twisting were adjusted until the geometry was acceptable. All parameters were adjusted for all end windings simultaneously, since an alteration in one affected the others. Contact proved difficult to avoid between phases while maintaining a realistic combination of twisting and bending, and several readjustments had to be made before a good result was achieved.

The design was also possible to model with cubic Bezier curves, which proved a much simpler task than with parametric curves, but due to reasons currently unknown, Comsol was not able to solve the FE problem with this geometry. The process was similar to the one described here, using curves for only half of the end winding and mirroring the resulting geometry. The Bezier curves were adjusted by weighing the four points defining the curve according to the wanted outcome. The same parameters for the shape of the coil were used, with the exception of s_b, since the sharpness of the curve could be adjusted with the weights of the Bezier curve. The curve used with this approach can be seen in Table V.

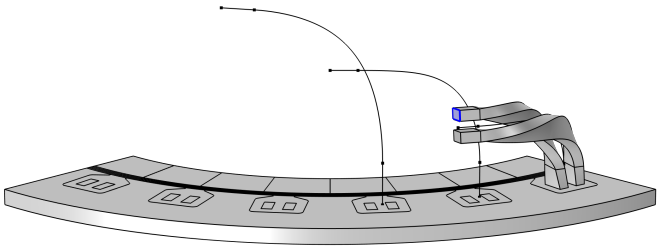

Fig. 12: Sweeping of end windings along parametric curves. Mirror surface indicated in blue.

3) Skewed saddle coil: Since the skewed coil was designed to be equal for all phases only the end winding of one phase needed to be modeled manually. The shape of a winding that is equal for all phases without overlapping other coils proved to be unnecessarily complex to model accurately with parametric curves, and cubic Bezier curves were therefore chosen for this winding. Two cubic Bezier curves were used to model the end winding, and no straight sections were included. The same parameters as for the rounded saddle coil, b, h, a and w_{mid}, were used, along with additional parameters for minor radius, b_1 and b_2, and height of bend, b_1 and b_2, for the respective curves. These were used to skew each curve in opposing directions. The parameter w_m was in this case used to contribute to the skewing, and indicates the x-coordinate where the two curves meet, i.e. the offset from the actual center of the end winding.

The cubic Bezier is defined by four points and four weights; by using the new radii and bend heights in the third and second points of the curve, setting a high b_1 and low h_1 for the first curve, and a high b_2 and low h_2 for the second curve, while using the original radius and height as a common coordinate in the fourth point for both curves, a skewed curve was achieved. For this to work properly, the two new parameters for each curve should be shifted with opposite signs with respect to the original height and radius, b. So that $\Delta b_1 \geq 0$ and $\Delta b_2 \leq 0$ when $\Delta b_i = b - b_i$, and the opposite for height, $\Delta h_1 \geq 0$

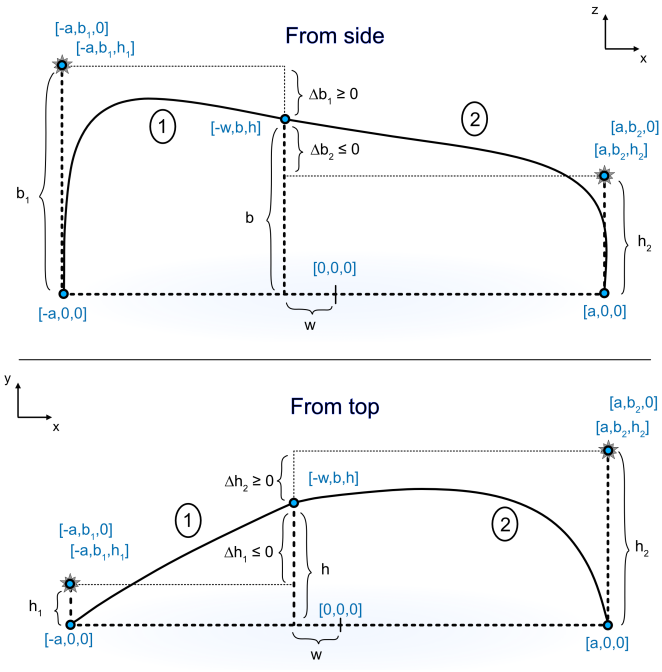

Fig. 13: Two dimensional view of Bezier curves with defined points seen from side and top. Points with star indicate two points located at different coordinates in 3rd dimension.

and $\Delta h_2 \geq 0$. As seen in Figure 13, only the end points are actually defined on the curve, while the two points in the middle are defined outside the curve, affecting the path between the end points and pulling the curve towards each of them. Adjusting the weight of a point determines how much the curve is pulled in the direction of each point.

TABLE V: Bezier curves

		Point	x	y	z	Weight
Rounded	**Curve**	P0	a	0	0	1
		P1	a	L_e	0	1.5
		P2	a	b	h	2
		P3	w	b	h	2.5
Skewed	**Curve 1**	P0	$-a$	0	0	2
		P1	$-a$	b_1	0	1
		P2	$-a$	b_1	h_1	1
		P3	$-w$	b	h	1
	Curve 2	P0	$-a$	0	0	2
		P1	a	b_2	0	1
		P2	a	b_2	h_2	2
		P3	$-w$	b	h	2

In the start, arbitrary values were used for the initial curves, and the major radius, a, and placement in slots were found in the same manner as for the rounded saddle coil. Again, the face of the coil within the slot was swept along the two curves with a twist factor. In the skewed winding, however, a constant twist factor gave an unlikely combination of twisting and bending. To adjust the twisting to fit the bending of

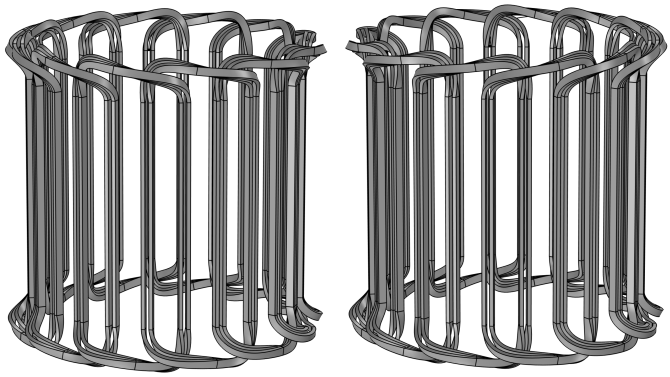

(a) Reverse end winding design used for analysis.

(b) Mirrored end winding without intertwined windings.

Fig. 14: Two possible versions of the skewed end winding.

the winding, a sine and cosine function was combined to a function, where the frequency of the waves were used to position the twist. The final twist function used was defined as $-s(0.725 - sin(s/600)cos(s/73))$, and was found through trial and error. In the skewed coil, both sections used the same function as twist factor, and the sweep could be conducted in a single operation for the two. Finally, the values were adjusted until the desired end winding design emerged, and the end winding was copied and rotated into the remaining slots. The final definition of the Bezier curves used can be seen in Table V. A full model was also made for this end winding design. It was decided to reverse the direction of the end winding for the other end of the machine, in an attempt to achieve a lower level of harmonics by avoiding mirroring of the end winding at both ends. This was done by simply sweeping the same curve in the opposite direction. This solution may give a lower harmonics, but it also means that all coils are intertwined, making it harder to produce the windings. The other solution with the mirrored geometry at both ends may be more prone to harmonics, but avoids this problem and would be easier to produce. A full set of windings of both designs can be seen in Figure 14.

V. 3D FEM Modeling of Rotating Machinery

FEM modeling of rotating machinery in three dimensions can be a time-consuming and meticulous task. This section aims to explain some relevant parts of the process by describing the methods used in this thesis, with some of the most common studies for rotating machines and the SCM described in section II as a reference point. The methods are based on a combination of experience from trial and error and advice from the COMSOL Support team. All models using the machine geometry were implemented with the physics module, *Rotating Machinery, Magnetic*, in Comsol Multiphysics.

In most cases, 3D models introduce an increased complexity compared to their 2D counterparts, and the number

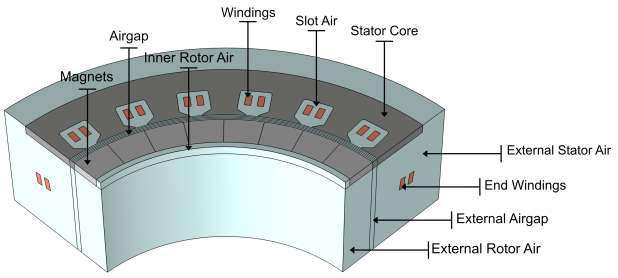

Fig. 15: Model including symmetric end winding.

of degrees of freedom in 3D FEA models can be vastly greater than that of equivalent 2D models. To mitigate the increased computational power needed, a mixed formulation is often used for 3D models of rotating machinery in Comsol, especially in the airgap where moving and stationary domains meet. This formulation was used to varying degrees in all models that includes the machine geometry throughout this thesis. All models used in the different studies are quite similar in geometry, materials, and formulations, but with some variations depending on what is required for the study in question. A quick overview of some formulations used for different studies is shown in Table VI. Other differences are mentioned when relevant.

TABLE VI: Study specific formulations

Machine part	Performance	Magnet Loss	End Windings	HTS loss/ behaviour
Windings	**A**	**A**	**A**	**T – A**
Stator iron	**A**	**A**	**A**	**A**
Stator air (slot)	**A**	**A**	**A**	**A**
Stator air (ext.)	**A**	**A**	**A**	**A**
Rotor air (ext.)	φ_m	φ_m	φ_m	φ_m
Rotor air (inner)	φ_m	φ_m	φ_m	φ_m
Magnets	φ_m	**A**	φ_m	φ_m
Air gap	φ_m	φ_m	φ_m	φ_m

The stator and rotor of the machine in this thesis feature the same cross-sectional geometry as the machine in [14], only extruded in the axial direction for 3D analysis. The stator of the machine is the same for all studies, except for variations in axial length. The names used in this thesis for different parts of the machine are labeled in Figure 15 for clarification.

A. Simplifications and assumptions

A perfect model of a machine is impossible to create, and using appropriate simplifications and assumptions is an important part of any modeling process. Some of the simplifications made for the models that were developed are listed here.

- Some machine aspects, such as magnet losses, back emf, and harmonics, can be modeled fairly accurately without using the complicated and computationally heavy superconductor formulations. Because of this, the windings are modeled as lossless superconductor coils, as described in [14].
- For the studies conducted in this thesis, the rotor back-iron holding is either neglected completely or modeled as air due to the assumption that a nonmagnetic material may be used in the final design.
- As in [14], the assumption is made that the machine is designed so that the BH-behaviour in the magnet takes place in the second quadrant of the hysteresis loop, according to [51], so that the hysteresis losses are negligible, and hence only the resistive losses are considered for the rotor magnets.
- The magnets are assumed to be electrically insulated from each other, and the induced current is therefore constrained within each magnet segment.
- Since there is no axial skewing in the designed machine, the axial and periodic symmetry of the machine allowed the model to be simplified to only a fraction of the actual machine geometry. To take advantage of the symmetry, only a quarter of the machine cross section is considered. The symmetry could be used cut down to an eight of the actual cross section with anti-periodic boundary conditions, but to include the end windings a quarter section is required, and using the same geometry makes comparison easier and allows for reuse of models. If the model is simplified further to an eight of the cross section, some effects may also be lost entirely if not fully symmetrical. Losses, for instance, were found to be greater for the north pole, as seen later in subsection V-C (Figure 26).
- To get the formulations to work correctly, all domains have to have non-zero values. Because of this, air domains were given a conductivity of $100\,\mathrm{S/m}$.

Some simplifications are more accurate than others, as is the case for the models developed for this thesis. Some of the assumptions initially made were inaccurate and led to models that gave unexpected results during studies, which in turn led to a change of method. Some of the errors made during the development of the models, along with solutions to the problems, are discussed in subsubsection V-F1.

B. Mixed formulation

Rotating Machinery, Magnetic in Comsol Multiphysics is based on a formulation that by default uses a combination of the magnetic vector potential, $\vec{A}$, and the magnetic scalar potential φ_m, to solve the 3D finite element problem [52]. In the context of the mixed formulation in this section, these are referred to as MVP and MSP, respectively. The formulation with, $\vec{A}$, is often called the **A**-formulation, which is described in more detail in the context of the **T-A** formulation in section III. A magnetic field with a nonzero curl where current

densities, or free currents, exist is described by the magnetic vector potential:

$$\vec{B} = \nabla \times \vec{A} \tag{28}$$

Using the magnetic scalar potential (MSP) is very effective for the case of modeling with permanent magnets, and is recommended in Comsol's guides for rotating machinery [53]. MSP is analogous to the electric scalar potential, also known as voltage, in that it is a scalar that can be used to indicate the amount of energy a magnetic charge would gain depending on its position in a magnetic field. There is, however, no magnetic voltage [54]; Unlike an electric charge, magnetic charges have not been proven beyond doubt to exist, as they would require a magnetic monopole. Magnetic monopoles are not considered completely outside of the realm of possibility, according to Nobel laureate, Paul Dirac, who originally made this abstraction in one of his famous contributions to quantum field theory, *Quantised Singularities in Electromagnetic Field* [20], earning them the name of "Dirac monopoles" in later years. The search for magnetic monopoles is still ongoing and has apparently been successful [55], but the lack of widespread attention globally indicates that the matter is not yet settled, and that if they do exist, they are extremely rare in nature [54].

Acting on the abstraction that magnetic charges do exist can provide a convenient and mathematically efficient way to represent the magnetic field. Considering the system as magnetostatic, by assuming that there are no free currents wherever the H-field exists, H becomes "curlless", $\nabla \times \vec{H} = 0$. It then follows that $\vec{H}$ should be derivable from the gradient of a potential, simply as:

$$\vec{H} = -\nabla V_m \tag{29}$$

Since there is no curl, there is no change in the field along its path, and thus the field can be represented as the gradient of a scalar [54]. This is not unlike what is done for the electric potential in an electrostatic system, where instead of a current-free system, the magnetic vector potential is assumed to be time-invarient, which leads eq. **??** to give only the electric potential (eq. 31):

$$\vec{E} = -\nabla V - \frac{\partial \vec{A}}{\partial t} \tag{30}$$

$$\frac{\partial \vec{A}}{\partial t} = 0 \Rightarrow \vec{E} = -\nabla V \tag{31}$$

What makes the magnetic scalar potential particularly useful is that it is defined by a single dependent variable as opposed to the three variables making up the components of the vector potential which significantly decreases the degrees of freedom solved for, and subsequently the computational efforts.

1) Implementation in Comsol: In order to solve the finite element problem in the boundary between the rotating and static domain, MSP should be used in the airgap domains on each side of the boundary. The implementation of the mixed formulation can vary depending on the problem, and the studies of interest; MSP is at the very least required in the domains on either side of the contact boundary between rotating and static domains, but can also be included in other domains where the dynamic behavior is less important, for instance in the magnetization of nonconducting magnets. Experience has shown that it is good practice to use MSP for all airgap domains, even if it is split into more than two radial segments, since there is no practical reason to model remaining parts of the airgap using vector potential, and a solution is found much faster. To avoid errors, MSP domains should preferably be connected within the same region to give accurate results [53].

For the magnetic scalar potential to be scaled correctly, a zero MSP point constraint must be placed at an appropriate point on the domains where MSP is used, as a point of reference. The constraint should be placed where the scalar potential can be assumed to be close to zero. Implementing zero MSP at an inappropriate point will result in large errors, as seen later in subsection V-C. To properly combine the formulations, a gauge transformation must be implemented. This transformation ensures that the scalar potential can be transformed into a vector field. Helmholtz's theorem says that a vector field is uniquely defined up to a constant if both $\nabla \cdot \vec{A}$ and $\nabla \times \vec{A}$ are given. To transform the scalar potential, both must be defined for the vector potential domains. $\nabla \times \vec{A}$ is defined in comsol by the default *Ampere's Law* node in the MVP domains, whereas the constraint on $\nabla \cdot \vec{A}$, has to be added manually. This constraint can be added with the *Gauge Fixing for A-field* node, which is defined as $\nabla \cdot \vec{A} = 0$. This particular constraint is also called the Coloumb gauge [52].

In some models, it is necessary to use two disconnected MVP domains, separated, for instance, by the MSP domain in the airgap. In this case, the same Gauge Fix should be applied to both MVP domains. The scalar potential is a scalar and does not contain information about the direction of the field. Using the same Gauge Fix on both domains enables information about the change in direction of the field to be transferred across the airgap, despite crossing into a scalar domain where this information would otherwise be lost. This enables the curl of the vector to be maintained, and allows a current density to be induced on one side of the airgap by a magnetic field originating from the opposite side.

The relevant nodes used to implement this formulation in Comsol Multiphysics are as follows:

- *Ampere's law:* used by default on all air domains belonging to the magnetic vector potential, and added as an additional node for the stator core to include the BH-constitutive relation for the magnetization model for this

specific domain.

- *Magnetic Flux Conservation:* used to model all air domains belonging to the magnetic scalar potential, this node does not include currents.
- *Coils:* A special case of Ampere's law, which was used in all the windings of the machine. The conductor model used was homogenized multiturn with a numeric coil type. The input and output boundaries are mostly self-explanatory and rely on the direction of the current, with the exception of the coil boundaries on the end windings that intersect the periodic boundaries as seen in Figure 15, where *Connected Boundaries* constraints are used to connect between the two periodic boundaries.
- *Conductive Magnet:* also a special case of Ampere's law, used to model the magnetization of the magnets with remanent flux. CM includes currents, which enables calculating resistive losses.
- *Nonconductive Magnet:* A special case of Magnetic Flux Conservation which was used to model the magnetization of the magnets through remanent flux density. Currents are not included and resistive losses cannot be found. Hysteresis losses are still possible with the correct magnetization model and material parameters. Both magnet nodes include the possibility of choosing a magnetization pattern. In the case of the Halbach array included here, it was implemented by choosing a north and south boundary for a single magnet and selecting a user-defined circular pattern. The circular pattern that describes the Halbach array in this case was $-2\pi/8$; one full revolution over 8 magnets.
- *Gauge Fixing for A-field:* a constraint on all MVP domains, required to couple magnetic vector and scalar potentials.

C. modeling for magnet losses

The magnet losses referred to here are the resistive heating losses caused by eddy currents in the magnets. The major difference for magnet loss analysis is that the magnets must be modeled as conductive magnets with the A-formulation. The **A**-formulation uses the time integral of the product of the electrical field and current density to calculate the resistive loss density according to eq. 32 [52]:

$$Q = \frac{1}{T} \int_{T_{end}-T}^{T_{End}} \vec{J} \cdot \vec{E} \; dt \tag{32}$$

The current density J, is found by the curl of the magnetic field strength :

$$\vec{J} = \nabla \times \vec{H} \tag{33}$$

In order to calculate the curl, all three directional components are needed, so the magnetic vector potential must be used in place of the scalar potential. Since the scalar potential was used in the airgap, and vector potential on either side, a single gauge fix was applied to the A-field for all domains with MVP. This enabled the current density required to find the resistive losses to be calculated.

The final method used to study the the magnet losses was the same as shown in Figure 19b. The same length of air domain and additional coil length was used, with the same placement of zero MSP constraint. The only difference between Figure 19b being the length of the stator segment, and the number and length of magnet segments included. The three models studied included $24\,\mathrm{mm}$ rotor and stator segments, with an additional $6\,\mathrm{mm}$ air domain and additional coil length. The length and number of segments for the different models used can be seen in Table VII.

TABLE VII: Segmentation of magnet loss models

Length	Segments	Magnets
6 mm	**4**	**32**
4 mm	**6**	**48**
2 mm	**12**	**96**

D. Modeling for End Winding effects

To study the effects of the end windings, the geometry seen in Figure 19b was expanded to include the end windings with a surrounding air domain. The formulation was similar to the one used for magnet loss, with the exception of the magnets. Magnet loss was not studied with the end windings, and nonconductive magnets with MSP were used instead. MVP and MSP were used in the additional air domains of the stator and rotor, respectively. The specific formulation used can be seen in Table VI.

Two different approaches were used for the end windings; The first using the same $6\,\mathrm{mm}$ segment as for performance studies to allow for comparison between the two winding designs and the "endless model", and to focus the computational efforts to the ends of the machine where the effects of end windings are most prevalent; The second was a full-length model of the machine, including both ends of the windings. Due to the difficulty in scaling values appropriately when studying only the end of the machine, the $6\,\mathrm{mm}$ segments were not used to estimate the overall performance. The was mainly focused on how the end of the machine was affected by the end windings and how end windings of different phases are affected by each other. The full-length model was used to study the distribution of the flux density in the axial length, and later used to estimate the performance of the machine. The strain experienced by the conductors was not modeled in this thesis, but a comprehensive analysis including strain computation in 3D with Comsol can be found in [56].

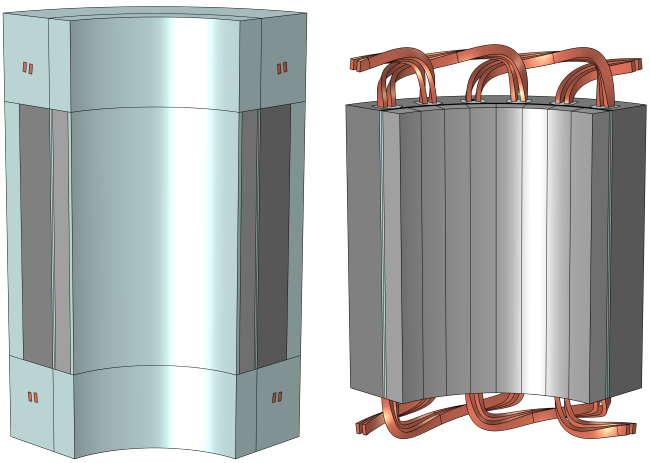

(a) All domains modeled. (b) End winding design.

Fig. 16: Full length machine model.

E. Model for performance

The full-length model including both end windings was used to investigate the torque and back-EMF in the machine. The model used the same formulation as previously mentioned for the end winding effects, and included the same external air domains in both ends of the machine (Figure 16b). Due to computational demands by the asymmetrical design, only the symmetrical winding was implemented in a full machine model.

The two ends of the windings were modeled in opposing directions in an attempt to achieve reduced cogging and overall harmonic interference. The two series connected coils in each slot were modeled as two separate closed loops to simplify the process.

To calculate the torque and power of the machine, the built-in interface for Arkkio's method in the *Rotating Machinery Magnetic* module in Comsol was used. With Arkkio's method, the torque of the rotor is found by calculating the surface integral of Maxwell's stress tensor over both the circumference and the length of the air gap, as shown in Equation 34 [57].

$$\tau_e = \frac{1}{\mu_0(r_o - r_i)} \int_{S_{ag}} r B_r B_\phi dS \tag{34}$$

where B_r and B_ϕ are the r- and ϕ-components of the flux density, and r is the radius of the integration path. For the machine models used to analyse the performance, the airgap was split into two domains, one on the rotating side of the model and one on the static side, with the surface between the two forming an identity pair for the *Moving Mesh* module. The radii of the two surfaces adjacent to the identity pair was used as the outer and inner radius for the radial integration path in Arkkio's method.

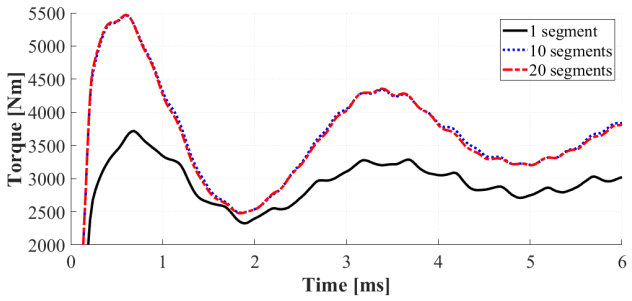

Fig. 17: (Torque over the first 2 electrical periods for full length model, for 1, 10 and 20 axial segments.

F. Investigation of errors

Errors were revealed while working on this thesis. Some of them have been fixed and others have not. The ones that are not fixed will be discussed further in section VII.

1) Stator segmentation in 3D models: When modeling the stator in a single domain, the torque was found to be much lower than expected. A test was therefore conducted with different segmentations, where the stator consisted of 10 and 20 axial segments. Due to the computational efforts involved for the full-length model, only the first two periods were compared for the test of stator segmentation.

From Figure 17 it can be seen that axial segmentation greatly influences the results. The average torque over the second period for the model with one segment was $3004\,\mathrm{Nm}$, while the models with 10 and 20 segments obtained an average torque of $3714\,\mathrm{Nm}$ and $3699\,\mathrm{Nm}$, respectively. For a number of 10 axial segments or above, the results are only marginally different. This indicates that there is minimum number of axial segments that should be used in the models when studying performance. This number is likely different for machines using different geometries, and should be obtained for each machine individually.

2) Inappropriate Zero MSP point: The mixed formulation using both MSP and MVP is not a perfect method for all models. The magnetic scalar potential requires a point of reference where its value is close to zero. When models do not include a domain where the potential can realistically be assumed to be zero during a full electrical period, such as in the air domain outside the stator or inside the rotor, this introduces a source of error.

In the early models used for the magnet loss analysis in this thesis, no outside domains were included, and MSP was thus only applied to the magnetic domain in the air gap of the machine, which in turn means that the zero MSP point must be applied somewhere within the air gap. For these models there was no point where zero MSP was an appropriate approximation, and an arbitrary point at the edge of a stator tooth was chosen. The potential at the stator teeth of a machine

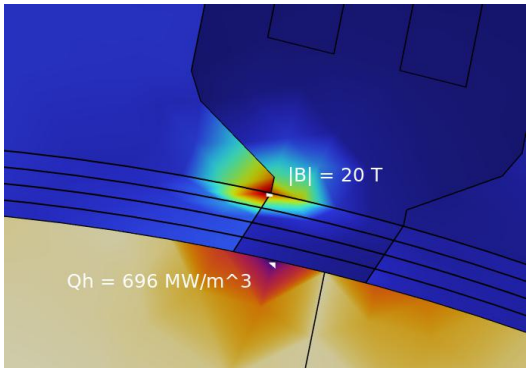

Fig. 18: Flux Density Norm and loss density around zero MSP point in airgap.

is far from zero during the greater part of the electrical period. The error could be seen as a significantly higher flux density than expected on the MVP domains around the point, which in turn led to a higher current density and magnet loss in the same area (Figure 18). The error was confined to a small area but may impact the overall results.

The impact of the error was investigated by comparing two models, one where no additional air domains are included (Figure 19a), and one where external air domains are added to one end of the machine segment (Figure 19b). In the model with external air, the coil domains were also extruded with the same length as the external air. This may impact the loss slightly, but as no steel surrounds this part of the coil, it is assumed that the flux density in the air gap remains more or less the same, and that an error caused by the additional coil length is much smaller than the error caused by a fault in the constraints. The placement of the zero MSP point constraint for the two models can be seen in Figure 19.

A simulation was run over two electrical periods. To eliminate the start-up effects of the solver, which often gives large errors during the first few time-steps, only the second period was used to evaluate losses. From the simulation, it was found that the two models had very different results for magnet losses. The average loss over the period was found to be $16.5\,\mathrm{W}$ for the model without external air domains, approximately 3.5 times the loss of the model with external air, $4.7\,\mathrm{W}$. The former also has a greater amplitude for the peak losses (Figure 20). The reason for this is likely the unrealistically high flux density caused by the inappropriate point constraint. If at all affected, the increase in losses from the additional stator length were negligible for the model with external air, compared to the error seen in the one without external air.

The error was found to be beyond what is acceptable and a solution in which zero MSP is placed in the airgap should not be used. To avoid this error in general, external domains, like the one in seenFigure 19b, can be added to all models where no point can be accurately estimated to have zero magnetic scalar potential.

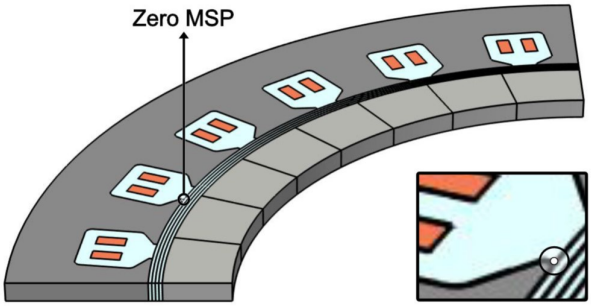

(a) Model without ext. air. MSP only in airgap, MVP on remaining domains, and conducting magnets. Method gave large magnet loss error, and should not be used.

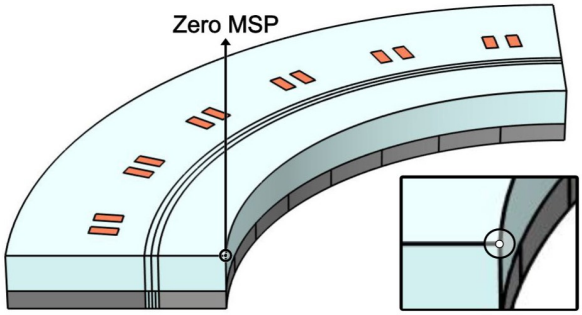

(b) Model with ext. air. MSP in airgap, ext. airgap and ext. rotor air.

Fig. 19: Models used to investigate placement of zero magnetic scalar potential constraint, and impact of external air domains.

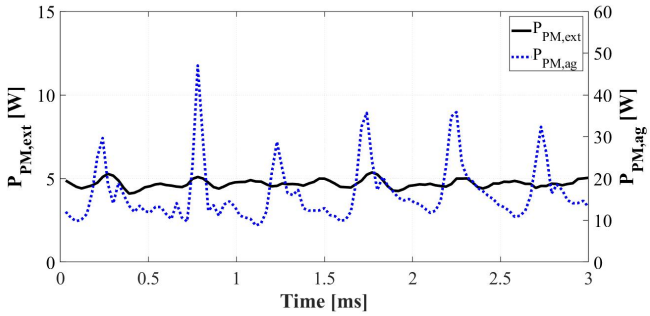

Fig. 20: Average heat loss in eight magnet segments of $6\,\mathrm{mm}$ (two poles) during one electrical period.

VI. 3D ANALYSIS OF SCM

This section contains an analysis of some interesting factors for the machine. The analysis starts with a quick look at torque, back EMF and flux distribution in the full-length model, before the end windings are studied with respect to the impact on the HTS tapes. Finally, a study of the magnet losses with

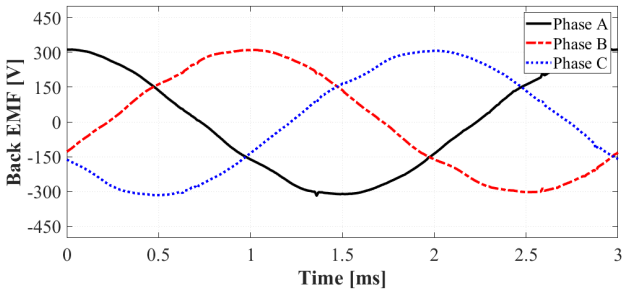

Fig. 21: Back EMF for 3rd electrical period.

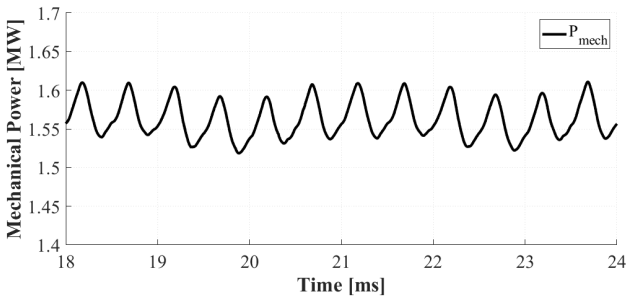

Fig. 22: Mechanical power in 7th and 8th electrical periods.

respect to axial segmentation length is conducted to conclude the analysis.

A. Full-length machine

It should be noted that no magnet segmentation or stator laminations were included in the full-length machine, which was later found to have a large impact on the mechanical power of the machine, causing a much lower power output. A transient behavior was observed for the first periods, leading to a focusing on the 6th to 8th electrical periods for the performance parameters, with the exception of Back EMF which was studied for the 3rd period, due to computation time. These topics are discussed further in section VII.

From Figure 21 it seems that the winding design provided a low level of harmonics. A slight perturbation can be seen approximately $0.4\,\mathrm{ms}$ before voltage peaks. There was also a small difference between the three in amplitude, which is likely a side effect of the aforementioned transient behavior since the swings are not fully dampened for during the 3rd period. The RMS values of phase A, B and C, were $217.9\,\mathrm{V}$, $214.2\,\mathrm{V}$ and $216.6\,$, respectively, and the average RMS value between the three was $E_{1,ph} = 216.2\,\mathrm{V}$.

The average torque was found to be $2985\,\mathrm{Nm}$ after the model could be said to have reached steady state in the time period between from the 6th to 8th electrical period, giving a mechanical power of $1.563\,\mathrm{kW}$ for the machine. This is much lower than what was found in [14]. It was later discovered that a higher power could be obtained by segmenting the stator, but the torque was still far lower than in [14] for the same magnetization and applied current.

A ripple of approximately 4.6% can be seen in the mechanical power (Figure 22), the number of peaks in the ripple corresponds to the number of slots traversed by the poles during the time period, and it is concluded that this is caused by the slotting and not the end winding design.

B. End Windings

Magnetic fields are known to negatively influence HTS tapes, reducing critical current density and increasing AC losses [18], [36], [58]. Because of the geometry of the tape, the field perpendicular to the face of the tapes will affect the critical limits more than any other direction. In [18], it was reported that the critical current can be reduced by 30-45%, depending on the field strength, for a perpendicular field compared to a field of the same intensity in the parallel direction. To study the potential impact of the end-winding designs on HTS tapes, the maximum flux density over time in the direction perpendicular to the tape face surface was investigated for all coil surfaces.

From Figure 24 it can be seen that the skewed coil is the end-winding design which is the least exposed to perpendicular fields. The perpendicular field is concentrated to certain areas of the coil, but the maximum value is lower than the rounded for close to the entire volume. The rounded saddle coil has a more evenly distributed $\vec{B}_{\perp}$-penetration, mostly centered in the width of the coil. The maximum perpendicular flux penetration in the normal directions for the rounded and skewed coils was $301\,\mathrm{mT}$ and $259\,\mathrm{mT}$, respectively. Experimental tests have shown that a difference of $42\,\mathrm{mT}$ in the maximum perpendicular field seen between the rounded and skewed coil, can reduce the critical current in tapes of the same type as used in the SCM here by over 10% [36]. Perpendicular fields are also the direction which gives the greatest Lorentz forces for a current carrying conductor. Lorentz forces are known to cause large damage on windings and the stator if not properly taken into account. Because of the large Lorentz forces involved in high current applications, and especially during short-circuit faults, flux shielding along with strong holding and damping mechanisms are often needed to deal with the mechanical stress caused by the extreme electromagnetic forces seen by the end windings in high speed applications, such as large turbogenerators [59], [60]. This could also be a challenge for the SCM in this thesis, since it is designed for the high speeds required for propulsion in aviation.

To obtain an estimate of the forces to which the end windings are exposed under normal operation, a calculation

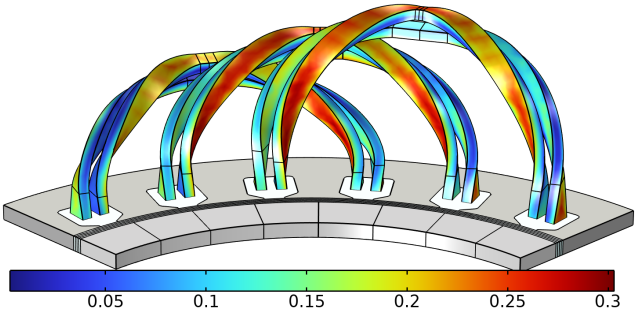

(a) Rounded saddle coil seen from inside of stator. $\vec{B}_{\perp}$ highest on inner surface closest to stator.

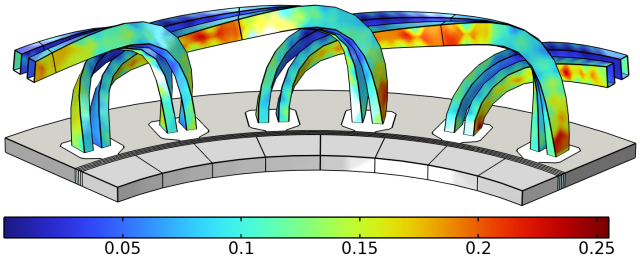

(b) Skewed saddle coil seen from inside of stator. Low overall $\vec{B}_{\perp}$, but more concentrated in center of coil and near slots.

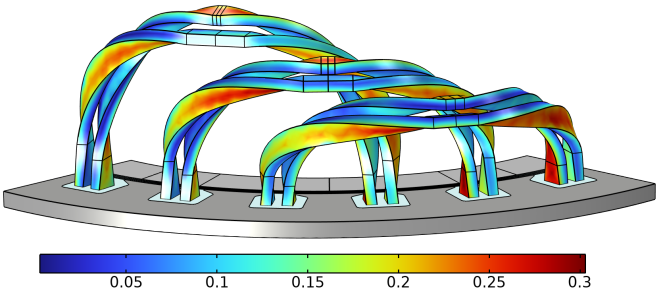

(c) Rounded saddle coil seen from outside of stator. $\vec{B}_{\perp}$ highest on outer surface in center of coils.

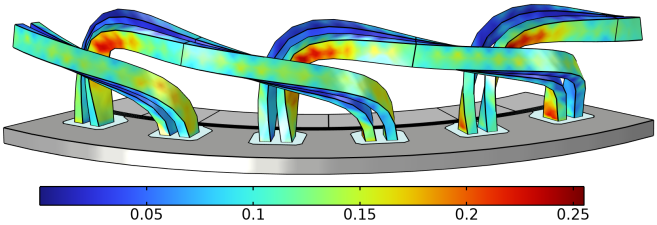

(d) Skewed saddle coil seen from outside of stator. High concentration of $\vec{B}_{\perp}$ around sharpest bend.

Fig. 23: Max flux density normal to tape faces, $\vec{B}\cdot\vec{n}$ or $\vec{B}_{\perp}$, on end windings. Calculated with $timemax(T_e l, 2{*}T_e l, rmm.Bx{*}nx + rmm.By{*}ny + rmm.Bz{*}nz)$ on the top and bottom, and $timemax(T_e l, 2*T_e l, rmm.Bx*t2x + rmm.By*t2y + rmm.Bz*t2z)$ on sides in Comsol.

of the Lorentz forces was undertaken. Comsol has built-in multiphysics modules for the calculation of Lorentz forces, but these require advanced coupling of mechanical and electromagnetic formulations that are not directly compatible with the *Rotating Machinery Module*, and which are not considered within the scope of this thesis. These modules must also be included and defined before simulations are run, which was not done here. Instead, a simple and fast method, specific for HTS tapes, was developed for the analysis of the end-winding designs previously presented. The magnetic force density can be found as the cross-product of the current density and the magnetic flux density:

$$\vec{F_L} = \vec{J} \times \vec{B} \tag{35}$$

The forces were investigated in Comsol by first looking at a time-step when the flux density normal to the surface was found to be the highest. Since the rounded coil was found to experience the greatest perpendicular field saddle coil, the forces were investigated for this end winding design, at the time-step $t = 52.7\,\mathrm{ms}$. The Curvilinear Coordinate method described in section III was then used to define the directions in terms of the geometry. Using the same thin strip approximation as for the **T-A** formulation, the current density was assumed to be only in the direction tangential to the flat surface of the conductors, and the field was only considered in the normal direction. With these assumptions, the force was calculated as:

$$\vec{F_{L,\mathbf{n}}} = (\vec{J}\cdot\vec{e}) \times (\vec{B}\cdot\vec{N}) \tag{36}$$

where $\vec{e}$ is the unit vector in the tangential direction, and $\vec{N}$ is the unit vector in the normal direction (domain normal, as required by Comsol). From Figure 24a it can be seen that the forces in the time-step are concentrated on the inner edge of the coil, and that the coils of phase C and B (left and center end winding, respectively) are pushed towards each other, while the two coils of phase C are forced in opposite directions. If not constrained properly by a holding mechanism, phase C and B will come in contact with each other due to the forces. These forces will also cause additional strains in the superconductors further reducing the critical values of field and current [17].

1) Flux distribution: From the full-length model with no axial segmentation, it can be seen that the ends of the machine have a large effect on the flux density in the stator in the radial and axial direction. The overall volumetric flux density is greater towards the ends of the machine than in the center, which can lead to greater losses in these areas Figure 25.

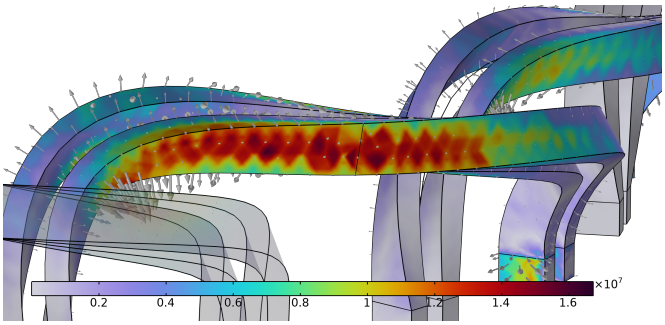

(a) Large concentration of $\vec{F_{L,\mathbf{n}}}$ pushing end winding towards stator, and the coils of the end winding towards each other.

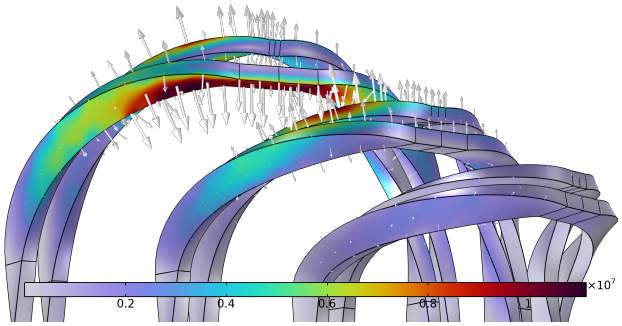

(b) $\vec{F_{L,\mathbf{n}}}$ pushing coils of phase C away from each other (left), and coils of phases B and C towards each other.

Fig. 24: Norm of volumetric force density, $|\vec{F_{L,\mathbf{n}}}|$, in rounded saddle coil at $t = 52.7\,\mathrm{ms}$. Force field, $\vec{F_{L,\mathbf{n}}}$, indicated by arrows. Units in $\mathrm{N/m^3}$.

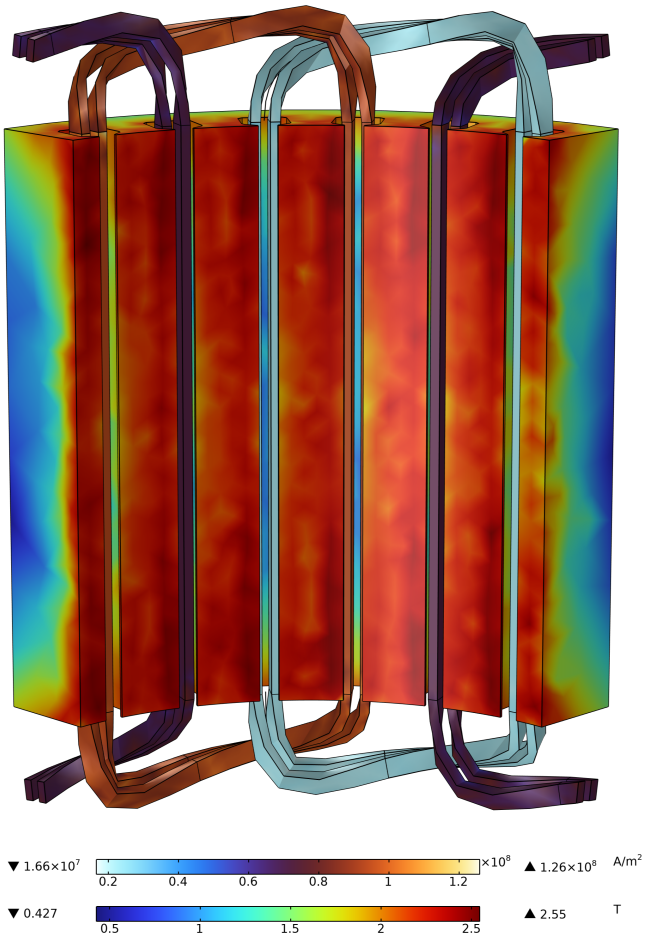

Fig. 25: Volume average of flux density in stator over one electrical period, and instantaneous current density in the coils.

C. Magnet losses and segmentation length

The magnet losses were found using models developed after the method described in subsection V-C. The models included an external air domain and additional coil length of $12\,\mathrm{mm}$ on one side of the machine segment. It is thought that this method also gives the opportunity to study some of the end effects on the magnets, since the coils are mostly straight immediately outside the slots. To investigate the effects of segmentation length, three models, all with a quarter machine section of $24\,\mathrm{mm}$, were studied with respect to resistive heating loss. The three models were made with segments of $6\,\mathrm{mm}$, $4\,\mathrm{mm}$ and $2\,\mathrm{mm}$, giving a total of 4, 6, and 12 axial segments, respectively (Figure 26).

1) Loss distribution: To find the loss distribution in the magnets, the average volumetric loss density over time was evaluated and plotted using built in functions in Comsol Multiphysics (Figure 26). For all segment lengths, the losses can be seen to be mostly concentrated in the end of the magnets facing the air gap, with close to zero losses on the bottom half, with the exception of the north pole in the $6\,\mathrm{mm}$ model. Losses are also higher on the edges of the magnet than in the center in all cases.

The instantaneous losses for all segments are visualized in Figure 28. The magnitude of the losses in each segment oscillates during the period, with a maximum peak near the end. The oscillations come in pairs with one larger and one smaller peak. There are 6 of these pairs, coinciding with the number of stator teeth traversed by the magnetic field during the period. The peaks of each pair also coincide with the entering and exiting of the stator teeth. The first peak occurs in the north pole immediately after its edge passes the previous tooth (Figure 27), and the second peak in the northwestern and southwestern magnet in the moment they enter and leave their respective teeth, which happens at the point when the north pole is parallel to the tooth. In both cases the loss is highest in the edges closest to the tooth.

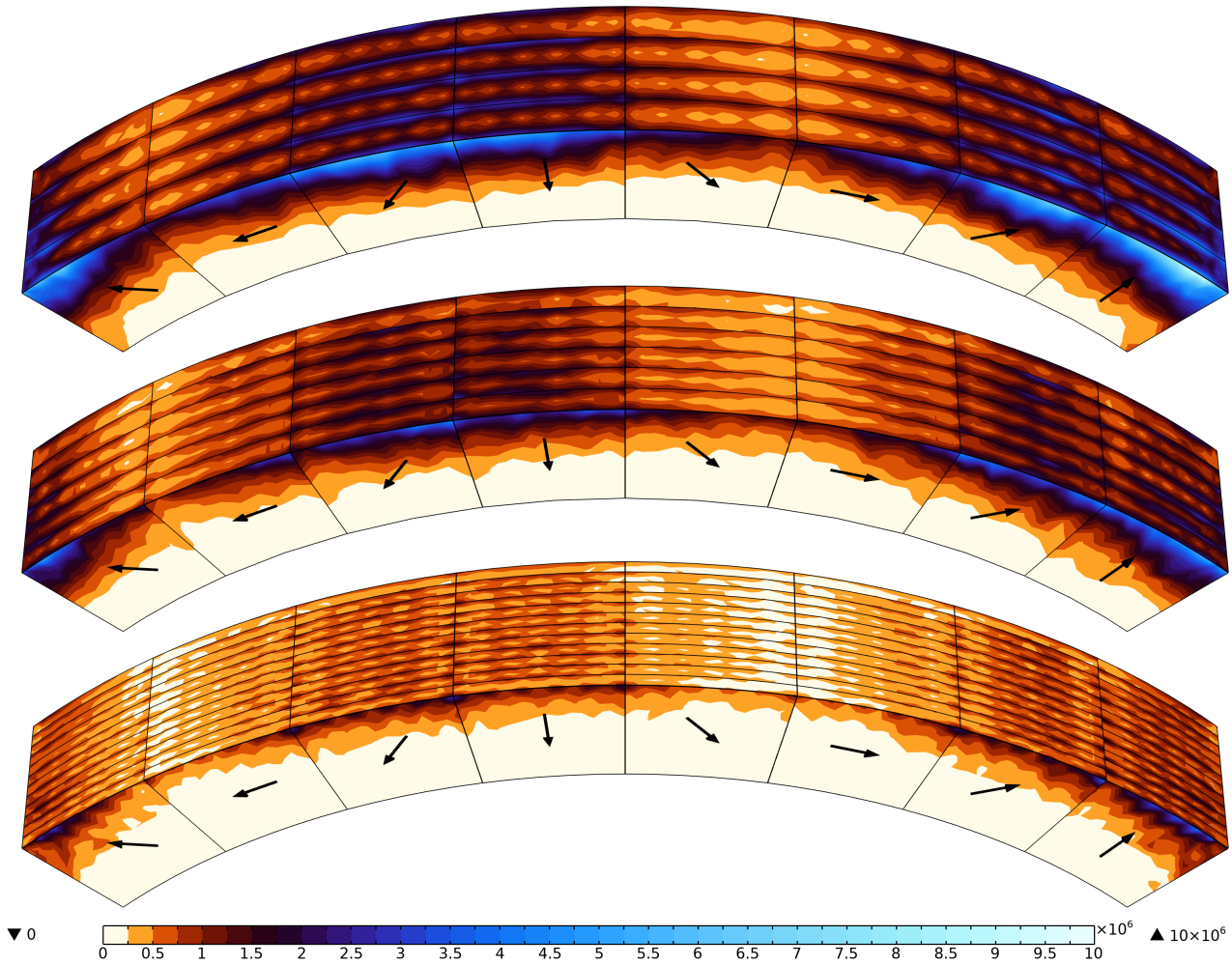

Fig. 26: Volumetric loss density averaged over time for quarter machine sections. 6 ,4 and $2\,\mathrm{mm}$ segment lengths from top to bottom, respectively. Loss density highest slightly ahead of north and south poles. Magnetization direction indicated by arrows (north, northwest, etc. from right to left). Rotation in counter clockwise direction, and air domain on side facing away.

Common for all models is that the peak of the oscillations are high but the midpoint is lower for the first segment, giving a lower overall loss than the second segment, despite the appearance. In the $6\,\mathrm{mm}$ model, the first segment has the lowest loss of all segments, and the losses in the remaining segments increase further from the top. For the models with $4\,\mathrm{mm}$ and $2\,\mathrm{mm}$, the loss is greatest for the second segment, while reaching a stable value after the fourth segment. In the $2\,\mathrm{mm}$ model, however, a decrease can be seen in the peaks for the final segment as well. It is thought that the magnet losses in the machine decreases toward the axial center, as the flux density is lower in this area than in the ends. It may be that a higher number of segments included $2\,\mathrm{mm}$ helps disperse the eddy currents fast enough to push this effect further towards the ends of the machine, giving reduced losses closer to the ends, and that this may be what is seen in Figure 28c. A further decrease in loss is expected for the next segments outside the $24\,\mathrm{mm}$ length modeled here, although how rapid a decrease is unknown. From Figure 25 it can be seen that the average flux density is lower in the axial center, which should indicate a lower loss for the magnets in this area. Figure 25 also shows a lower flux density at the very top of the machine, and a higher flux density immediately below the top, which coincides well with the magnet losses found in the top segments. Based on this reasoning, a clear reduction in losses should be seen for segments between the $100\,\mathrm{mm}$ from both ends, which may be observed if a longer axial length is included in the models.

With respect to the magnetization direction, the same behaviour was observed in all three models. The losses were found to be mostly concentrated around the poles, with the highest average loss on the north pole, and slightly lower in the northwest and northeast segments, closest on either side. The loss in around the south pole was found to be much lower than the north, and skewed towards the west, giving the highest loss in the southwestern segment for this area. This could be the result of an error with the phase shift of the current, where

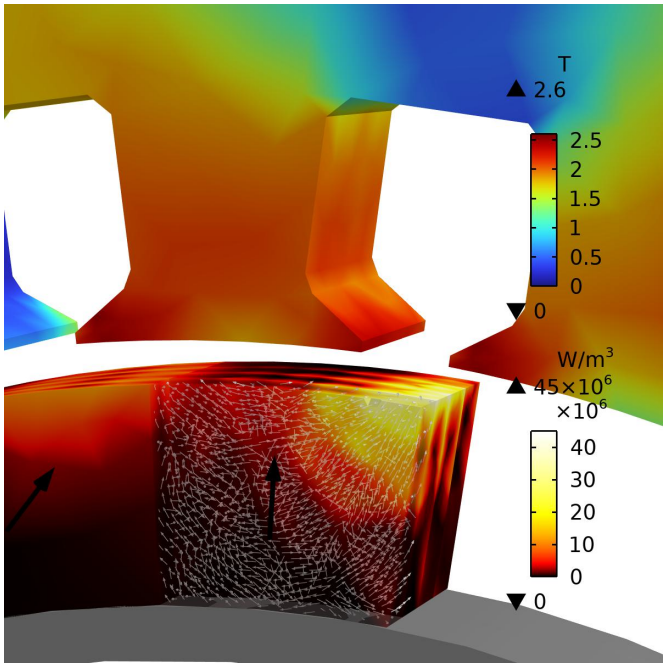

Fig. 27: Peak in instantaneous loss density immediately after north pole has left stator tooth (rotation in counter clockwise direction). Circulating eddy currents in the north pole magnet indicated by white arrows.

it has not been 100% lined up in the q-axis direction. A slight skewing is also seen around the north pole in the opposite direction. This may also be caused by a dependence on the rotational direction, and an interaction between the direction of the flux and velocity vectors in the airgap, leading losses to be slightly higher as some magnets enter the vicinity of the stator teeth than when they leave, and vice versa.

The total loss in each segment was found by numerically integrating the average loss in all time steps over the electrical period, using the trapezoidal method, and dividing by the total length of the time period. The resulting losses can be seen in Table VI-C1. The loss observed over the north pole segment was 65%, 49%, and 52% higher than the average loss in all segments of the 2 mm, 4 mm, and 6 mm models, respectively. A shorter segment length is found to reduce the losses significantly. For the 24 mm length of the machine studied, the 4mm and 6mm had a loss that was 92 and 180% greater than the 2mm long segment. The difference between the lengths also seems to increase further further from the end of the machine. For the first 12 mm of the machine, the losses in the 4mm and 6mm were 80 and 153% greater, while in the second the difference increased to 104 and 209%, respectively.

2) Estimation of total magnet loss in machine: The difference between the segmentation length is far from negligible, and shorter segments seem preferable to longer with respect to resistive losses. The final decision is, however, made based on a wider range of factors, such as cost and practicability.

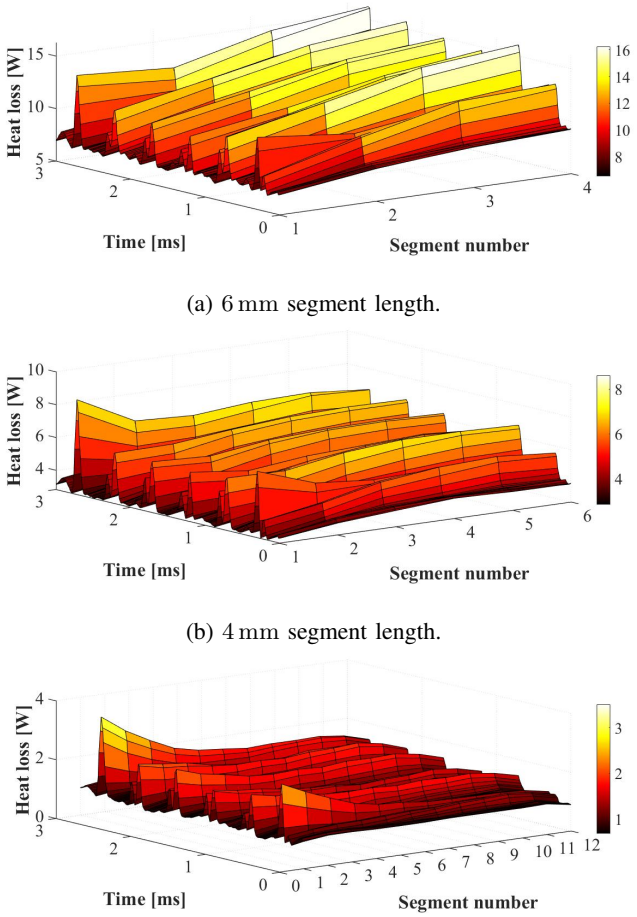

(a) 6 mm segment length.

(b) 4 mm segment length.

(c) 2 mm segment length.

Fig. 28: Resistive heat loss per segment during one electrical period. Numbering starts from side of external air domain. Only one pole pair, or 8 magnet segments are included.

Despite being the most efficient, the sheer number of magnets required when using 2 mm long segments, may prove too expensive depending on the type of magnet required. To give some indication of some benefits from which to weigh the cost, the total losses in the machine was found for each segment length.

For the first 24 mm of each end of the machine, the values in Table VIII were used directly. The number of segments included in from the study was too small to make a realistic prediction of the reduction of loss toward the axial center of the machine. Because of this, loss in the remaining segments of the machine was assumed to be equal to the final segment studied, i.e., the 12th segment for the 2 mm model, etc. The estimated losses found with this method are listed in Table IX, along with the number of magnets required in each case.

The total estimated magnet losses are very low, in the range of 0.02 - 0.07 % of the rated power found in 2D analysis by Mellerud Et Al in [14]. The loss and number of axial segments

TABLE VIII: Resistive loss in magnet segments and poles

Halbach section	Segment length 2 mm	4 mm	6 mm
N	8.327 W	14.458 W	21.521 W
NE	6.062 W	12.209 W	17.607 W
E	3.222 W	6.691 W	9.711 W
SE	2.797 W	5.557 W	7.981 W
S	5.110 W	10.227 W	14.881 W
SW	5.378 W	10.843 W	15.778 W
W	3.488 W	7.374 W	10.786 W
NW	5.848 W	9.976 W	14.634 W

Segment	Segment length 2 mm	4 mm	6 mm
1st	1.067 W	3.606 W	7.734 W
2nd	1.150 W	4.049 W	9.169 W
3rd	1.140 W	4.384 W	10.138 W
4th	1.110 W	4.567 W	10.648 W
5th	1.106 W	4.625 W	
6th	1.121 W	4.548 W	
7th	1.122 W		
8th	1.143 W	**All segments**	
9th	1.154 W		
10th	1.167 W	**6 mm**	37.646 W
11th	1.144 W	**4 mm**	25.778 W
12th	0.997 W	**2 mm**	13.411 W

TABLE IX: Total magnet losses in machine

Segment length	6 mm	4 mm	2 mm
Total magnet loss	1664.5 W	1079.4 W	490.2 W
Number of magnets	1280	1920	3840

in the machine are close to exponentially inversely related. Following the trend, a further 50% reduction in magnet loss in the machine would require close to double the amount of magnets.

VII. Discussion

A. Neumann Condition for *T-A* formulation

The Neumann Condition was, as mentioned in section III, suspected to be the main issues in the implementation of the **T-A** formulation. Several variations of the Neumann conditions were tested with different source terms, g, some of which are listed here:

- $T \cdot N_x + T \cdot N_y + T \cdot N_z$
- $(T \cdot N_x)n_x + (T \cdot N_y)n_y + (T \cdot N_z)n_z$
- $E_x \cdot N_x + E_y \cdot N_y + E_z \cdot N_z$
- $E_x \cdot n_x + E_y \cdot n_y + E_z \cdot n_z$
- $(E_y \cdot N_z - E_z \cdot N_y) + (E_z \cdot N_x - E_x \cdot N_z) + (E_x \cdot N_y - E_y \cdot N_x)$
- $(E_y \cdot N_z - E_z \cdot N_y)n_x + (E_z \cdot N_x - E_x \cdot N_z)n_y + (E_x \cdot N_y - E_y \cdot N_x)n_z$
- 0 (Equal to zero flux)

where $\vec{n}$ was the surface normal in Comsol and $\vec{N}$ is the domain normal defined by CC. It is believed that TN_x should be able to represent the x component of $\vec{T}$ in eq(24), when only the components in the normal direction are considered $T_x = T \cdot N_x$. It should also be mentioned that to use the electric field at a boundary, the field must be redefined by using the tangential derivative operator,"*dtang*", in comsol instead of the usual "*d*"-operator, i.e. $\vec{E} = \rho(\nabla \times (T \cdot \vec{N}))$ had be recalculated for surfaces.

All of the inputs seemed to give the same outcome: A solution could not be found when horizontal mesh elements were included in the model, and internal mesh nodes were void of equations; When only vertical mesh elements were included, a solution was found for the external boundaries, but the same solution was found regardless of the input to g in the *Flux/Source* node. The error indicated that the **T**- and **A**-formulations were not correctly coupled since $\vec{T}$ was undefined within the superconducting domain. Due to limited time, no further attempts were made at solving this issue.

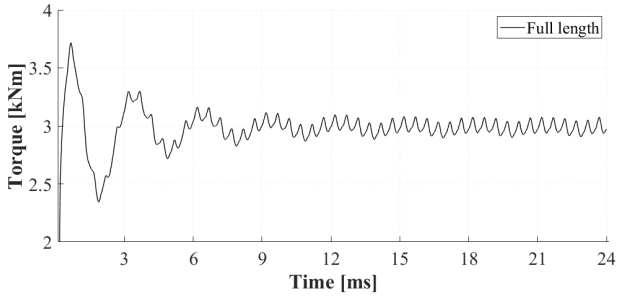

Fig. 29: (Torque over the first 8 electrical periods for full length model (no stator segments). Transient torque considered dampened after approximately 6 periods.

B. Transient behavior in 3D models

A transient behavior was observed for the 3D models using nonconducting magnets with the magnetic scalar potential. This transient was in the form of a dampened sine wave oscillating around the steady state value. The oscillations were prevalent for the first few electrical periods, before dampened to a point where the system reached steady state operation. This was unexpected as it is not observed in 2D models using the same parameters, [14]. However, when conducting magnets were included through the magnetic vector potential this was not the case, and steady state was achieved from the first period.

The reason for this is not known, but it may be that there is a low amount of inherent dampening in the system when nonconducting magnets are used, and that including the conducting magnets increases the dampening significantly by removing energy in the form of losses. The swings seemed to disappear for short segments when air domains were included, but remained in the full-length model.

VIII. Conclusion

In this thesis, methods and formulations for the development of 3D models for the study of rotating machinery were presented. Models were developed for a superconducting machine for aviation, which was used as a case study for the implementation of the methods and formulations presented. To investigate the potential for implementation of superconductor formulations to model the electromagnetic behavior of the HTS tapes in windings, the 3D homogenized **T-A** formulation was tested in a replication study of [18] was attempted. A useful method of defining a custom coordinate system with curvilinear coordinates was described and implemented for the purpose of the **T-A** formulation, this method allowed normal and tangential components to be defined within a domain, which is not possible in Comsol by default. This also simplified post-processing significantly when looking at fields perpendicular to the tapes. A limited time-frame and an issue with a Neumann Boundary Condition led to the prioritization of other aspects, and the replication was finally abandoned as an unsuccessful attempt. The formulation and and its implementation was described in detail in order to enable future correction of errors.

Two end windings were designed and developed for the machine to address some of the aspects missing from 2D models. One was a rounded saddle coil, and the other was a skewed and twisted saddle coil. The skewed coil was compact and rotationally symmetrical in a distributed winding layout, while the rounded coil was found to be more fitting for a concentrated layout. The formulae and method used to develop the end windings were presented, along with a general formula for a saddle coil, which provides a good way of modeling the turns of a coil in great detail. The implementation of the mixed φ_m-**A** formulation in the *rmm* module in Comsol was studied with respect to different machine aspects considered. Here, it was found that the scalar potential φ_m should be used in all airgap domains, and that external air domains were needed on the outer boundaries representing the axial ends of the machine to achieve a reliable results. The correct placement of the Zero MSP point and Gauge Fix were also found to be paramount for models using the mixed formulation. Machines modeled with non-conducting magnets were found to have a transient component that was not seen with conducting magnets. The models and formulations described were then used for analysis.

An analysis of the impact of the end winding designs undertaken. A full-length machine model with the skewed end winding design was used to calculate the torque, back EMF, and flux distribution in the stator. The skewed end winding provided a smooth and close to sinusoidal back EMF, with a relatively low harmonic component. The low visible component was suspected to stem from a combination of the more prevalent cogging due to slotting in the stator and transient behavior, and not from the end windings. A slight shift in the amplitude of the different phases was seen, which was concluded to be due to the transient component from the non-conducting magnets used in the model. The flux density in the machine showed a higher concentration towards the axial ends, which indicates a flux leakage from the end windings. $6\,\mathrm{mm}$ axial machine segments were used to study the impact of the different winding designs on the HTS tapes in the coils. The maximum field perpendicular to the tape surface was found to be highest for the rounded coil which also had its maximum field evenly distributed along its length, suggesting that the end windings experience high Lorentz forces during the whole electrical period. In the skewed saddle coil, the perpendicular field was concentrated in two areas for all time steps, suggesting that it experiences lower forces for a greater part of the electrical period. To investigate the Lorentz forces in greater detail, a simple and fast method of calculating the Lorentz forces for HTS tapes was developed using the Curvilinear Coordinate system implemented for the **T-A** formulation, and the thin-strip assumption from the same formulation. Both end windings were studied for a time-step when perpendicular B-field was high. Calculations showed that the norm of the field visible on the surfaces was in fact higher for the on the skewed end winding was in fact higher than for the rounded saddle coil, but the vector field, however, was greater for the saddle coil. The vectors indicated that the coils are pushed in unfavourable directions in the end windings, and that there is a need for rigid holding structures for these.

Finally, the magnet losses were studied with respect to axial segmentation in the Halbach array of the rotor. Three different segmentation lengths of 2,4 and $6\,\mathrm{mm}$ were compared for an axial machine segment of $24\,\mathrm{mm}$. The results showed a close to inversely exponential relationship between the height of the segments and the losses. The total losses in the whole machine segment was lowest for the $2\,\mathrm{mm}$ magnet segments at $490.2\,\mathrm{W}$, while the losses for the 4 and $6\,\mathrm{mm}$ were 92% and 180% higher, respectively. In the azimuthal direction, the losses were found to be heavily skewed towards a few magnets, with the north pole having the highest losses, at 49-$65\,\%$ above the average for all magnets, depending on the axial segment length.

IX. Further Work

- The magnetic scalar potential caused a transient behavior when used in the rotor magnets, and the impact of non-conducting vs. conducting magnets on performance should be studied in greater detail.
- The steps of the **T-A** formulation should be reviewed, corrected, and implemented for the end winding models developed to include HTS losses.
- A study should be conducted to investigate whether the end winding designs are realistic in practice. Improvements are possible for the winding designs, and optimization of the design with respect factors like flux leakage, harmonics and Lorentz forces should be conducted.

Lorentz force calculations should also be expanded to include the skewed end windings, as well as a more in-depth study of the saddle coil. The forces may create the need for alterations to the end winding design, which should be discovered early in the process. Other possible variations of the designs were also tested, such as the mirrored skewed coil seen of Figure 14b in section IV, were also made for the machine and should be tested.

- The minimim number of axial stator segments needed for a consistent torque should be obtained for the model, to minimize the computational efforts.
- The magnet segments indicated that the losses are thought to be decreased further from the top. A decrease could be seen, but a stable value was not reached, which led to the conclusion that this decrease would continue if a machine segment longer than $24\,\mathrm{mm}$ was studied. A study should therefore be conducted to investigate how many magnets and how long a machine segment is necessary to capture the full behavior in the machine.

X. Acknowledgements

I would like to show my gratitude to my supervisor Jonas K. Nøland for giving me the opportunity to study and work with a topic that I find incredibly interesting. I also want to thank Michiel Desmedt for giving me initial pointers on 3D modeling, saving me several hours of work. Finally, I want to thank my co-supervisors, Runar Mellerud and Christian Hartmann for helpful advice and discussions over the last year, and a special thanks to Runar for his great supervisory work, for supplying me with good references and putting me in contact with the right people, and for always encouraging and pushing me throughout the year.

References

[1] "Aviation leaders report 2023: New horizons," jan 2023. [Online]. Available: https://assets.kpmg.com/content/dam/kpmg/ie/pdf/2023/01/ie-aviation-leaders-report-2023-new-horizons.pdf

[2] *Profitability and the air transport value chain*, ser. IATA ECONOMICS BRIEFING, vol. 10. International Air Transport Association, june 2013. [Online]. Available: https://www.iata.org/en/iata-repository/publications/economic-reports/profitability-and-the-air-transport-value-chain/

[3] "Global outlook for air transport: Highly resilient, less robust," june 2022. [Online]. Available: https://www.iata.org/en/iata-repository/publications/economic-reports/global-outlook-for-air-transport----june-2023/

[4] Airbus, "Hybrid and electric flight | Airbus," Jul. 2021, section: Innovation. [Online]. Available: https://www.airbus.com/en/innovation/low-carbon-aviation/hybrid-and-electric-flight

[5] "Electric Skies: Boeing Joins GE And NASA's Hybrid Electric Flight Project | GE News." [Online]. Available: https://www.ge.com/news/reports/electric-skies-boeing-joins-ge-and-nasas-hybrid-electric-flight-project

[6] J. K. Nøland, C. M. Hartmann, and R. Mellerud, "Next-generation cryo-electric hydrogen-powered aviation: A disruptive superconducting propulsion system cooled by onboard cryogenic fuels," *IEEE Industrial Electronics Magazine*, pp. 2–11, 2022.

[7] G.-D. Nam, L. D. Vuong, H.-J. Sung, S. J. Lee, and M. Park, "Conceptual design of an aviation propulsion system using hydrogen fuel cell and superconducting motor," *IEEE Transactions on Applied Superconductivity*, vol. 31, no. 5, pp. 1–7, 2021.

[8] J. K. Noland, R. Mellerud, and C. Hartmann, "Next-Generation Cryo-Electric Hydrogen-Powered Aviation: A Disruptive Superconducting Propulsion System Cooled by Onboard Cryogenic Fuels," *IEEE Industrial Electronics Magazine*, vol. 16, no. 4, pp. 6–15, Dec. 2022. [Online]. Available: https://ieeexplore.ieee.org/document/9786856/

[9] "Superconductivity," Jun. 2023. [Online]. Available: https://home.cern/science/engineering/superconductivity

[10] H. S. Shin, "Review of progress in electromechanical properties of REBCO coated conductors for electric device applications," *Progress in Superconductivity and Cryogenics*, vol. 16, no. 4, pp. 7–16, Dec. 2014. [Online]. Available: https://doi.org/10.9714/PSAC.2014.16.4.007

[11] Y.-H. Zhou, D. Park, and Y. Iwasa, "Review of progress and challenges of key mechanical issues in high-field superconducting magnets," *National Science Review*, vol. 10, no. 3, p. nwad001, Mar. 2023. [Online]. Available: https://doi.org/10.1093/nsr/nwad001

[12] T. E. Union. (2022) Clean aviation. [Online]. Available: https://clean-aviation.eu/

[13] E. Commission, D.-G. for Mobility, Transport, D.-G. for Research, and Innovation, *Flightpath 2050 : Europe's vision for aviation : maintaining global leadership and serving society's needs*. Publications Office, 2011.

[14] R. Mellerud, C. Hartmann, C. Klop, and J. K. Nøland, "Design of a Power-Dense Aviation Motor with a Low-Loss Superconducting Slotted Armature," preprint, Jul. 2023. [Online]. Available: https://www.techrxiv.org/articles/preprint/Design_of_a_Power-Dense_Aviation_Motor_with_a_Low-Loss_Superconducting_Slotted_Armature/23612001/1

[15] R. Mellerud, J. Nøland, and C. Hartmann, "Preliminary design of a 2.5-mw superconducting propulsion motor for hydrogen-powered aviation," in *2022 International Conference on Electrical Machines (ICEM)*, 2022, pp. 1404–1410.

[16] S. Austad and E. A. Aabrekk, "Development of terminations and experimental testing methods for hts tapes," 2022.

[17] Hyung-Seop Shin, Su-Yong Choi, Dong-Kyun Ko, Hong-Soo Ha, Dong-Woo Ha, and Sang-Soo Oh, "A comparison of strain effect on critical current in Bi-2223 superconducting tapes in different bending modes," *IEEE Transactions on Appiled Superconductivity*, vol. 13, no. 2, pp. 3526–3529, Jun. 2003. [Online]. Available: http://ieeexplore.ieee.org/document/1212389/

[18] C. R. Vargas-Llanos, F. Huber, N. Riva, M. Zhang, and F. Grilli, "3D homogenization of the T-A formulation for the analysis of coils with complex geometries," *Superconductor Science and Technology*, vol. 35, no. 12, p. 124001, Dec. 2022. [Online]. Available: https://iopscience.iop.org/article/10.1088/1361-6668/ac9932

[19] S. Superconductors. (2022) Second generation high temperature superconducting tape. [Online]. Available: http://www.shsctec.com/index.php?m=list&a=index&classid=62

[20] A. K. Jha and K. Matsumoto, "Superconductive rebco thin films and their nanocomposites: The role of rare-earth oxides in promoting sustainable energy," *Frontiers in Physics*, vol. 7, 2019. [Online]. Available: https://www.frontiersin.org/articles/10.3389/fphy.2019.00082

[21] F. Trillaud, G. dos Santos, and G. G. Sotelo, "Essential material knowledge and recent model developments for rebco-coated conductors in electric power systems," *Materials*, vol. 14, no. 8, p. 1892, 2021.

[22] B. Shen, "Study of second generation high temperature superconductors: Electromagnetic characteristics and ac loss analysis," Cham, 2020.

[23] S. Narayana, Y. Polyakov, and V. Semenov, "Evaluation of flux trapping in superconducting circuits," *IEEE transactions on applied superconductivity*, vol. 19, no. 3, pp. 640–643, 2009.

[24] T. Oka, A. Takeda, H. Oki, K. Yamanaka, L. Dadiel, K. Yokoyama, W. Häßler, J. Scheiter, N. Sakai, and M. Murakami, "Magnetic flux trapping and flux jumps in pulsed field magnetizing processes in rebco and mg-b bulk magnets," *Journal of Physics: Conference Series*, vol. 1590, no. 1, p. 12025, 2020.

[25] A. K. Geim, I. V. Grigorieva, S. V. Dubonos, J. G. S. Lok, J. C. Maan, A. E. Filippov, and F. M. Peeters, "Phase transitions in individual sub-micrometre superconductors," vol. 390, no. 6657, pp. 259–262. [Online]. Available: http://www.nature.com/articles/36797

[26] A. A. Abrikosov, "Type ii superconductors and the vortex lattice - nobel lecture," 12 2003.

[27] C.-L. Song and Q.-K. Xue, "Cuprate superconductors may be conventional after all," vol. 10, p. 129. [Online]. Available: https://link.aps.org/doi/10.1103/Physics.10.129

[28] P. Anderson, "Theory of flux creep in hard superconductors," *Physical review letters*, vol. 9, no. 7, pp. 309–311, 1962.

[29] W. P. Crump, "On the nature of self-field critical current in superconductors and its use as a probe of the superfluid density," 12 2021. [Online]. Available: https://openaccess.wgtn.ac.nz/articles/thesis/On_the_nature_of_self-field_critical_current_in_superconductors_and_its_use_as_a_probe_of_the_superfluid_density/17134880

[30] H. Zhang, M. Zhang, and W. Yuan, "An efficient 3D finite element method model based on the *T–A* formulation for superconducting coated conductors," *Superconductor Science and Technology*, vol. 30, no. 2, p. 024005, Feb. 2017. [Online]. Available: https://iopscience.iop.org/article/10.1088/1361-6668/30/2/024005

[31] S. Li and E. Pardo, "Numerical modelling of soldered superconducting REBCO stacks of tapes suggests strong reduction in cross-field demagnetization," *Scientific Reports*, vol. 13, no. 1, p. 1087, Jan. 2023. [Online]. Available: https://www.nature.com/articles/s41598-023-27996-4

[32] V. M. R. Zermeño and F. Grilli, "3d modeling and simulation of 2g hts stacks and coils," *Superconductor science technology*, vol. 27, no. 4, pp. 44 025–7, 2014.

[33] A. Kario, M. Vojenciak, F. Grilli, A. Kling, B. Ringsdorf, U. Walschburger, S. I. Schlachter, and W. Goldacker, "Investigation of a rutherford cable using coated conductor roebel cables as strands," *Superconductor science technology*, vol. 26, no. 8, pp. 85 019–6, 2013.

[34] Y.-F. Zhao and T.-H. He, "Kim Model of Transport ac Loss with Position Dependent Critical Current Density in a Superconducting Cylinder," *Journal of Low Temperature Physics*, vol. 159, no. 3, pp. 515–523, May 2010. [Online]. Available: https://doi.org/10.1007/s10909-010-0160-0

[35] A. Crisan, "On a modified Kim-Anderson model of the current-voltage characteristics of high-temperature superconducting ceramics," *Journal of Superconductivity*, vol. 7, no. 4, pp. 687–691, Aug. 1994. [Online]. Available: https://doi.org/10.1007/BF00721648

[36] X. Zhang, Z. Zhong, J. Geng, B. Shen, J. Ma, C. Li, H. Zhang, Q. Dong, and T. A. Coombs, "Study of Critical Current and n-Values of 2G HTS Tapes: Their Magnetic Field-Angular Dependence," *Journal of Superconductivity and Novel Magnetism*, vol. 31, no. 12, pp. 3847–3854, Dec. 2018. [Online]. Available: https://doi.org/10.1007/s10948-018-4678-8

[37] F. Huber, W. Song, M. Zhang, and F. Grilli, "The T-A formulation: an efficient approach to model the macroscopic electromagnetic behaviour of HTS coated conductor applications," *Superconductor Science and Technology*, vol. 35, no. 4, p. 043003, Apr. 2022. [Online]. Available: https://iopscience.iop.org/article/10.1088/1361-6668/ac5163

[38] W. Hong, H. Liu, F. Liu, H. Jin, and S. Yi, "Improved Calculation of Magnetic Hysteresis Loss of Stacked Superconducting Cable Under T-A Formulation," *IEEE Transactions on Applied Superconductivity*, vol. 32, no. 6, pp. 1–5, Sep. 2022, conference Name: IEEE Transactions on Applied Superconductivity.

[39] S. Wang, H. Yong, and Y. Zhou, "Calculations of the AC losses in superconducting cables and coils: Neumann boundary conditions of the T–A formulation," *Superconductor Science and Technology*, vol. 35, no. 6, p. 065013, May 2022, publisher: IOP Publishing. [Online]. Available: https://dx.doi.org/10.1088/1361-6668/ac6a52

[40] X. Xu, Z. Huang, W. Li, X. Huang, M. Wang, Z. Hong, and Z. Jin, "3D finite element modelling on racetrack coils using the homogeneous T-A formulation," *Cryogenics*, vol. 119, p. 103366, Oct. 2021. [Online]. Available: https://www.sciencedirect.com/science/article/pii/S0011227521001247

[41] K. Goda, N. Amemiya, T. Nakamura, Y. Mori, T. Ogitsu, T. Kurusu, and M. Yoshimoto, "A novel magnet design using coated conductor for spiral sector ffag accelerators," *IEEE Transactions on Applied Superconductivity*, vol. 24, no. 3, pp. 1–5, 2014.

[42] K. Koyanagi, S. Takayama, T. Tosaka, K. Tasaki, T. Kurusu, T. Yoshiyuki, N. Amemiya, and T. Ogitsu, "Development of saddle-shaped coils using coated conductors for accelerator magnets," *IEEE Transactions on Applied Superconductivity*, vol. 23, no. 3, pp. 4 100 404–4 100 404, 2013.

[43] K. Mizuno, M. Sugino, and M. Ogata, "Experimental production and evaluation of racetrack coils for rebco on-board magnet," *Quarterly Report of RTRI*, vol. 57, no. 3, pp. 234–239, 2016. [Online]. Available: https://www.jstage.jst.go.jp/article/rtriqr/57/3/57_234/_article

[44] D. Sekiguchi, T. Nakamura, S. Misawa, H. Kitano, T. Matsuo, N. Amemiya, Y. Ito, M. Yoshikawa, T. Terazawa, K. Osamura, Y. Ohashi, and N. Okumura, "Trial test of fully hts induction/synchronous machine for next generation electric vehicle," *IEEE Transactions on Applied Superconductivity*, vol. 22, no. 3, pp. 5 200 904–5 200 904, 2012.

[45] T. Nakamura, T. Dong, J. Matsuura, T. Kiss, K. Higashikawa, S. Sato, and P. Zhang, "Experimental and theoretical study on power generation characteristics of 1 kw class fully high temperature superconducting induction/synchronous generator using a stator winding with a bending diameter of 20 mm," *IEEE Transactions on Applied Superconductivity*, vol. 32, no. 6, pp. 1–5, 2022.

[46] B. Liu, R. Badcock, H. Shu, and J. Fang, "A superconducting induction motor with a high temperature superconducting armature: Electromagnetic theory, design and analysis," *Energies*, vol. 11, no. 4, 2018. [Online]. Available: https://www.mdpi.com/1996-1073/11/4/792

[47] A. Mikhailichenko and T. Moore, "Simple procedure for superconducting coil winding," in *PACS2001. Proceedings of the 2001 Particle Accelerator Conference (Cat. No.01CH37268)*, vol. 5, 2001, pp. 3645–3647 vol.5.

[48] H.-S. Shin, S.-Y. Choi, D.-K. Ko, H.-S. Ha, D.-W. Ha, and S.-S. Oh, "A comparison of strain effect on critical current in bi-2223 superconducting tapes in different bending modes," vol. 13, no. 2, pp. 3526–3529.

[49] J. W. van der Laan, D C; Ekin, "Dependence of the critical current of yba 2 cu 3 o 7δ coated conductors on in-plane bending," *Superconductor Science and Technology*, vol. 21, no. 11, p. 115002, 2008. [Online]. Available: https://browzine.com/articles/41539714

[50] M. Takayasu, L. Chiesa, L. Bromberg, and J. V. Minervini, "HTS twisted stacked-tape cable conductor," *Superconductor Science and Technology*, vol. 25, no. 1, p. 014011, dec 2011. [Online]. Available: https://doi.org/10.1088/0953-2048/25/1/014011

[51] J. Pyrhönen, S. Ruoho, J. Nerg, M. Paju, S. Tuominen, H. Kankaanpää, R. Stern, A. Boglietti, and N. Uzhegov, "Hysteresis Losses in Sintered NdFeB Permanent Magnets in Rotating Electrical Machines," *IEEE Transactions on Industrial Electronics*, vol. 62, no. 2, pp. 857–865, Feb. 2015, conference Name: IEEE Transactions on Industrial Electronics.

[52] C. Support, "Comsol multiphysics 6.1 reference manual," 2023. [Online]. Available: https://doc.comsol.com/6.1/doc/com.comsol.help.comsol/comsol_ref_introduction.16.04.html

[53] N. Paudel, "Guidelines for modeling rotating machines in 3d," 2016. [Online]. Available: https://www.comsol.com/blogs/guidelines-for-modeling-rotating-machines-in-3d/

[54] H. A Hause and J. R. Melcher, *Electromagnetic Fields and Energy*. Boston, Massachusetts, US: Massachusetts Institute of Technology, 1998.

[55] M. W. Ray, E. Ruokokoski, S. Kandel, M. Möttönen, and D. S. Hall, "Observation of dirac monopoles in a synthetic magnetic field," *Nature*, vol. 505, no. 7485, pp. 657–660, Jan. 2014.

[56] Y. Pan and P. Gao, "Analysis of mechanical behavior and electromechanical properties of REBCO-coated conductor tapes under combined bending-tension loads using numerical methods," *Superconductor Science and Technology*, vol. 36, no. 4, p. 045006, Feb. 2023, publisher: IOP Publishing. [Online]. Available: https://dx.doi.org/10.1088/1361-6668/acbac7

[57] A. Arkkio, "Analysis of induction motors based on the numerical solution of the magnetic field and circuit equations," Helsinki, 1987.

[58] S. Li and E. Pardo, "Numerical modelling of soldered superconducting REBCO stacks of tapes suggests strong reduction in cross-field demagnetization," *Scientific Reports*, vol. 13, no. 1, p. 1087, Jan. 2023. [Online]. Available: https://www.nature.com/articles/s41598-023-27996-4

[59] Y. Zhao, W. Huo, C. Zeng, C. Chen, and Y. Ma, "Dynamic response of large turbogenerator stator end winding under fault conditions," *Journal of Physics: Conference Series*, vol. 1074, p. 012030, Sep. 2018. [Online]. Available: https://iopscience.iop.org/article/10.1088/1742-6596/1074/1/012030

[60] X. Wen, R. Yao, and J. Tegopoulos, "Calculation of forces on the stator end windings of turbogenerator by the transient quasi-3D method," *IEEE Transactions on Magnetics*, vol. 32, no. 3, pp. 1669–1672, May 1996, conference Name: IEEE Transactions on Magnetics.

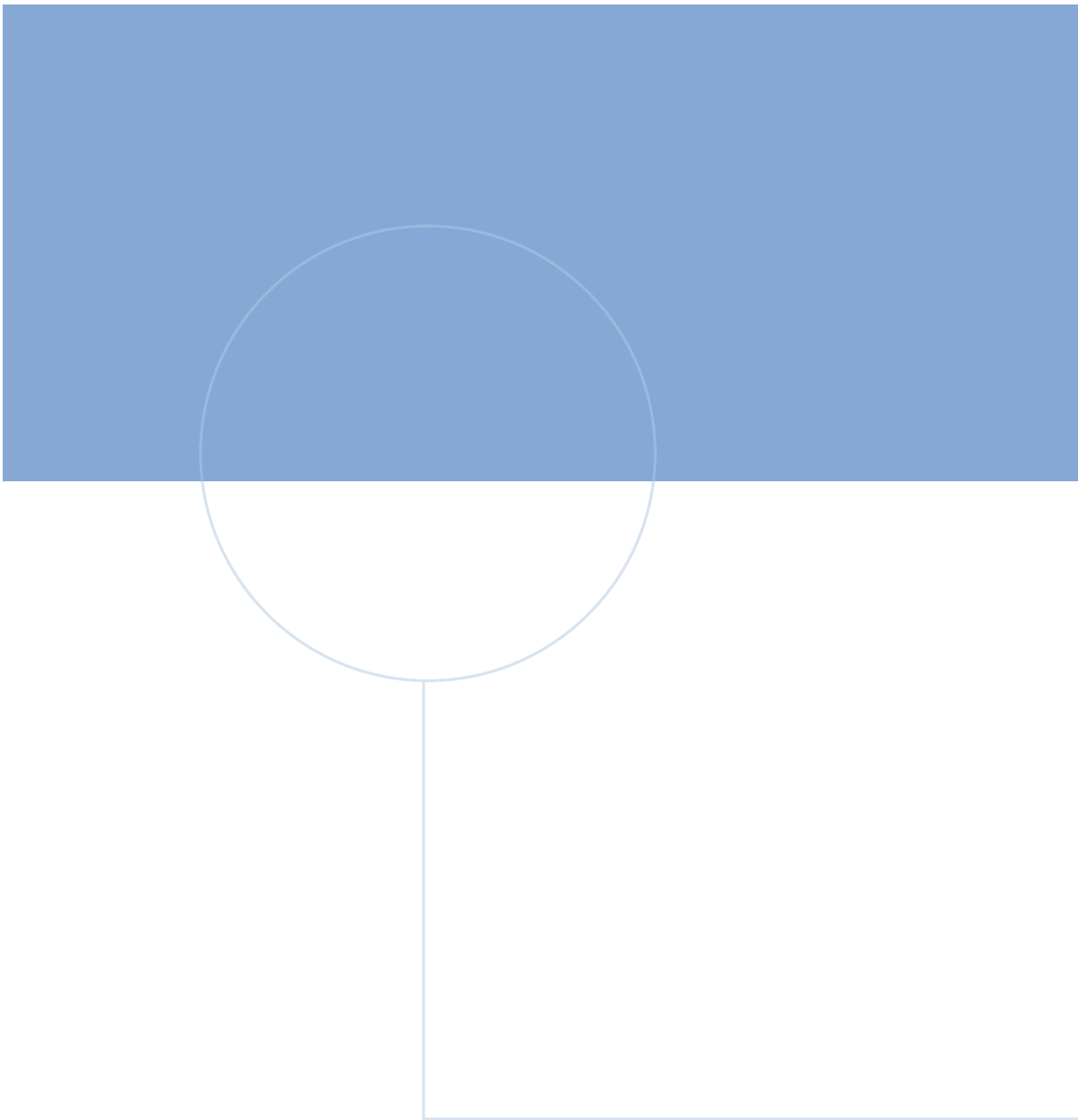

NTNU

Norwegian University of
Science and Technology